INVESTIGATION OF SCALING EFFECTS DUE TO VARYING DIELECTRIC MATERIALS IN ASYMMETRIC SURFACE DIELECTRIC BARRIER DISCHARGE ACTUATORS

By

ALVIN NGO

Bachelor of Science in Aerospace Engineering

University of Oklahoma

Norman, Oklahoma

2015

Submitted to the Faculty of the
Graduate College of the
Oklahoma State University
in partial fulfillment of
the requirements for
the Degree of
MASTER OF SCIENCE
July, 2017

INVESTIGATION OF SCALING EFFECTS DUE TO VARYING DIELECTRIC MATERIALS IN ASYMMETRIC SURFACE DIELECTRIC BARRIER DISCHARGE ACTUATORS

Thesis Approved:

Dr. Jamey D. Jacob

Thesis Adviser

Dr. Brian R. Elbing

Dr. Arvind Santhanakrishnan

ACKNOWLEDGEMENTS

I would like to thank the follow people:

Immediate family – For being my most needed distraction and support system.

- Cynthia Ngo
- Man Ngo
- Nancy Ngo

Thesis advisor – For guiding me through pretty much every aspect of this work and for bringing me a salad when I needed it.

- Dr. Jamey Jacob

Acquaintances and Consultants – For aiding with pieces of advice or providing small distractions to help distress.

- Jordan Feight (main contributor)
- Kedar Pai (main contributor)
- Chris Petrin (PIV teacher)
- Solmoz Azartash-Namin
- Dr. Jim West

Committee members – For taking time out to give me feedback on my thesis.

- Dr. Brian Elbing
- Dr. Arvind Santhanakrishnan

Friends – For being my least needed distractions and support system.

- Geoffrey Donnell
- Sandro Gomarteli
- Spencer Huynh
- Daniel Karami
- Johnson Ong

Name: Alvin Dinh Ngo

Date of Degree: JULY, 2017

Title of Study: INVESTIGATION OF SCALING EFFECTS DUE TO VARYING DIELECTRIC MATERIALS IN ASYMMETRIC SURFACE DIELECTRIC BARRIER DISCHARGE ACTUATORS

Major Field: MECHANICAL AND AEROSPACE ENGINEERING

Abstract:

To understand completely the range of uses for asymmetric surface dielectric barrier discharge (SDBD) actuators, a thorough knowledge of how geometrical, material, and interactional changes affect the actuator is necessary. Previous studies have determined a large selection of efficient and effective geometrical and interactional configurations, but a complete analysis of the dielectric materials used to buffer between the two electrodes of the asymmetric SDBD configuration has yet to materialize. By testing SDBD actuators with differing dielectric materials, dielectric thicknesses, and electrode gap distances, a comparative analysis of their effects on the plasma actuator's induced body force are performed. Using optical image analysis (OIA) and particle image velocimetry (PIV), the plasma regime and induced body force created by the actuators are observed. Multiple PIV scenarios are used to discern not only the mean flow field, but also to obtain velocity measurements from the induced body force. Increased thickness and gap distance are observed to have similar effects on the induced body force in a constant current scenario. Increasing dielectric constant is seen to have a significant negative impact on the plasma generated in a constant current scenario. Through a combination analysis between these two methods, a higher efficiency actuator is worked towards from these three parameters setting up future work on potential propulsive purposed plasma actuators.

TABLE OF CONTENTS

Chapter Page

Chapter Page

LIST OF FIGURES

LIST OF TABLES

CHAPTER I

INTRODUCTION

1.1. Motivation

From a possible means of alternative thrust for unmanned aerial systems to sterilization and decontamination of medical equipment, the range of uses for plasma seems only limited by the unorthodox means necessary to apply it. By understanding various geometrical parameters' effects on a plasma actuator, the strong induced flow and specific plasma species generation for bacteria eradication becomes feasible. To pull plasma further into the world of applicability, a certain level of optimization is required. Various studies have been performed to observe the scaling effects of electrode dimensions, power, and frequency in regards to plasma volume and geometric modifications, but the full definition of what parameters can display trends for plasma actuators has yet to be fully explored [2]. One potential avenue of discovery lies in the dielectric material. This buffer between the electrodes is what defines many of the characteristics of plasma being generated, i.e., plasma species generated, dielectric thickness to achieve a certain output of plasma, maximum voltage input, etc. [3].

1.2. What is an asymmetric single SDBD?

The specific means to produce plasma that will be discussed throughout this work is through an asymmetric single surface dielectric barrier discharge actuator. Dielectric barrier

discharge was chosen because the process is non-thermal, has no moving parts, has a variety of sizes and shapes, and requires relatively low power. The actuator is of the surface variety rather than the volumetric variety because of the induced body force that is provided due to the entrainment of the flow near the actuator. Only single actuators will be discussed due to their simplistic nature with multiple actuators pending in future works. And finally the asymmetric case will be analyzed rather than the symmetric case because of higher plasma concentration in one area. Each of these aspects will be discussed further in Chapters II and III.

1.3. Goals and Objectives

The main goal of this work is the observation of the effects due to varying the dielectric material (and specific properties) and changing the gap distance between the electrodes on specific SDBD actuator. This is performed in hopes of achieving higher efficiency plasma actuators in terms of induced flow strength and plasma regime control. Various methods will be applied and tested to see if they are viable for future works, especially the combination of their analyses. Optical image analysis (OIA) and Particle image velocimetry (PIV) will be employed on the many actuator cases each with specific objectives. The objective of OIA is to provide a method of observing plasma uniformity and streamer onset as input voltage is increased. The objective of PIV is to observe the mean flow field and determine the momentum transfer into the induced flow. A combination of these analyses will provide a stronger understanding of how the above mentioned variations in SDBD actuators affects their induced flow output and efficiency as a whole.

1.4. Thesis Outline

The thesis will start with a brief background on plasma and the things that characterize and classify it. Specificity increases throughout Chapter II and flows into the scaling of this specific type of actuator in Chapter III. The scaling chapter will discuss previous research done in scaling the actuators along with other potential means to scale them. Several key parameters will be defined and an overview of the efficiency of these actuators will be given. Fundamental ±s that govern

these calculations along with limitations of the upcoming system will be noted here. The experimental arrangements follow suit in Chapter IV and Chapter V. The arrangements along with their individual analyses are split into their respective methods: optical image analysis and particle image velocimetry. A summary of results will be presented in Chapter VI along with a combination of the analyses and the conclusions they yield. Finally, at the end of Chapter VI is a collection of possible future works in the case of expanding or continuing this research. The references and appendices follow the conclusions section.

CHAPTER II

BACKGROUND

2.1. Fundamentals of Plasma

Considered the fourth state of matter, plasma is a hot ionized gas that has an equal amount of positive and negative charges. Unlike neutral gases however, plasma is made up of electrically charged particles that are easily influenced by electric and magnetic fields. The Greek term plasma was first used to describe this phenomenon by Tonks and Langmuir in 1929 [30]. From a thermodynamic standpoint, plasma is easily described using phase transitions. Commonly known, solids, liquids, and gases are differentiated by the strength of their particles' bonds. By increasing the thermal energy of a solid or liquid material, the particles will overcome the binding potential energy resulting in a phase transition. These transitions happen at a constant temperature and at a given pressure. If more energy is provided, a molecular gas will gradually dissociate into an atomic gas due to the increased collisions in the system. At some point of increased temperature, the gas becomes ionized, meaning the binding energy of the outermost orbital electrons has been overcome. This shift is not a phase transition as seen between solids, liquids, and gases, but rather it happens gradually and with increasing temperature. This ionized gas state is plasma.

Plasma is formally defined by three criteria: macroscopic neutrality, Debye shielding, and

plasma frequency [30]. Macroscopic neutrality refers to plasma maintaining a net resulting electric charge of zero. This is observed under several conditions: no external forces, the volume must be large enough to contain a non-insignificant amount of particles, and the volume must be small in comparison to the characteristic lengths for variation of macroscopic parameters (density and temperature). Essentially, the inner regions of the plasma hold microscopic space charge fields that cancel each other out. Debye shielding is easily described using the characteristic length of plasma known as *Debye length*. This is the distance over which the influence of charged particles is felt by other particles within the plasma. As the plasma particles accumulate, a shielding of the electrostatic fields is observed. The Debye length is defined as

$$\lambda_d = \left(\frac{\epsilon_0 kT}{n_e e^2}\right)^{\frac{1}{2}} \tag{1}$$

where ϵ_0 is the permittivity of free space, k is Boltzmann's constant, T is the temperature, n_e is the density of electrons, and e is the charge of an electron. Debye shielding effect is a characteristic of all plasma in which all physical dimensions of the system must be large compared to λ_D [30].

This leads into a quantity known as the plasma parameter, which is defined by

$$g = \frac{1}{n_e \lambda_D^3} \tag{2}$$

This quantity when much less than 1 is called the plasma approximation and is the ratio between interpaticle potential energy and the mean plasma kinetic energy. The last parameter is the plasma frequency. This is the stability of the macroscopic space charge neutrality. When disturbed, plasma attempts to return to its neutral state. The natural frequency of the oscillations created in this motion is known as the plasma frequency. For example, imagine a plasma at rest that is disturbed by an external force. The plasma's charge is altered and the force is removed instantaneously. The internal electric field will work to maintain neutrality, but due to inertia it

will overshoot neutrality and begin producing an electric field in the other direction. This will continue until equilibrium is reached through the rate of plasma frequency which eventually yields a macroscopically neutral plasma.

2.1.1. Types of Plasma

Plasma are generally classified as either thermal or non-thermal. Many plasmas exist in nature as seen in Figure 1a-c. The majority of matter in the known universe exists as a plasma [30]. Stars, with the closest one being the sun, is made from plasma. Based off of thermonuclear fusion reactions, the high temperatures in stars cause constant thermonuclear reactions maintaining the stars' gaseous form. This also means that a majority of plasmas that exist are thermal. Thermal plasmas, or hot plasmas, are produced in high pressure discharges. Though they exist abundantly they do not possess easily harnessable traits. Non-thermal plasmas, or cold plasmas, are formed in low pressure discharges or in short pulse discharges, as in dielectric barrier discharges. There is, however, a third type of plasma known as warm plasma. They are easiest explained using definitions for the hot and cold plasmas. Cold plasmas do not take temperature into account and thus the average velocity of electrons in a small mass of plasma is the velocity of all electrons inside the small mass. Hot plasmas, in contrast, do take into account temperature. Thus complicating their electron velocities causing them to not follow any previous assumptions. Warm plasmas historically stand somewhere in between. Depending on the intensity of the temperature, or essentially the speed at which the electrons move, warm plasma or hot plasma models are used in place of cold plasma models [17]. This work will focus on non-thermal plasmas.

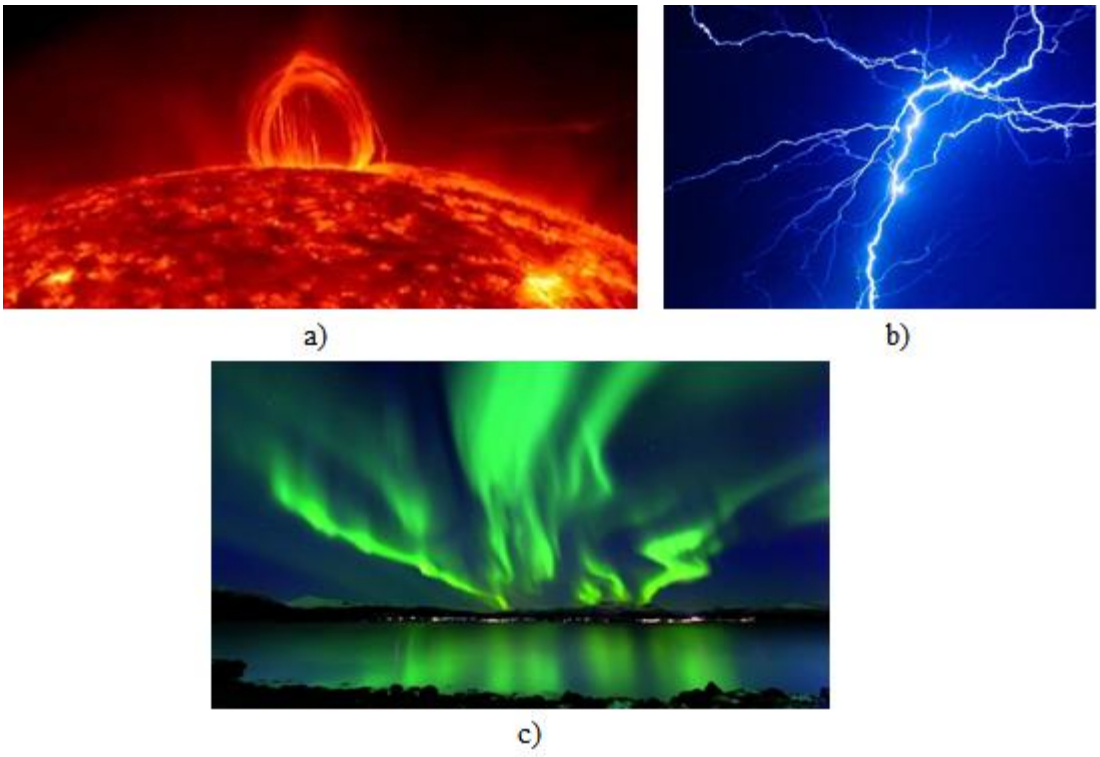

Figure 1. Illustrations of plasma examples: a) the Sun, b) lightning, and c) Aurora Borealis [26-28].

2.1.2. Cold Plasma Production

Cold plasmas have been used in various biomedical applications reaching but not limited to the inactivation of bacteria, the loosening of connections between cells in biological tissue, the coagulation of blood to reduce the bleeding of a wound, and even potentially the removal of cancerous tumors [31]. A large amount of research performed on cold plasmas has been dedicated to biological purposes. The name "cold plasma" is slightly misleading because it is only named so because it is colder than their counterparts. Technology has reached the point, however, that certain cold plasma applications are cool enough for human skin to handle as seen in Figures 2 [31]. In addition to the previous applications, plasmas have also been used for aerospace purposes, such as flow control and noise reduction [1]. This work stands to enlighten and back the necessary research in pushing cold plasma applications to aerospace purposes, specifically using surface dielectric barrier discharge. One widely used means of creating plasma is known as

dielectric barrier discharge (DBD) which is seen in Figure 2. Cold plasma can be created through various means. Specifically, cold atmospheric plasma (CAP) has taken the spotlight in medicine as cutting edge technology in the form of DBDs, atmospheric pressure plasma jets (APPJ), plasma needles and even a plasma pencil. The relatively low temperatures combined with the utility involved with these plasmas allow them to be open to research and development. Their main resistance is the amount of voltage required to power them. For the purposes of aerospace propulsion and flow control, dielectric barrier discharge is a potential candidate that leads cold plasmas into the world of unmanned aerial systems (UAS) and other aircraft. This work centers its focus on DBDs as a possible avenue for this purpose.

A strong reason for DBDs flexibility is its ability to be used in atmospheric air. Previous work have shown that DBDs can create reactive species in atmospheric air that work well for microbial inactivation. Additionally, the zero-net-mass flux device that is SDBD actuators can generate its own flow by producing plasma in atmospheric air. Due to the impact (inelastic and elastic collisions) between electrons, ions, and neutral atoms that are moved by the electric field reactive species are created. The excitation and dissociation of different molecules also adds to this. Due to the high concentrations of nitrogen and oxygen in atmospheric air, various active species may be formed, i.e., ozone.

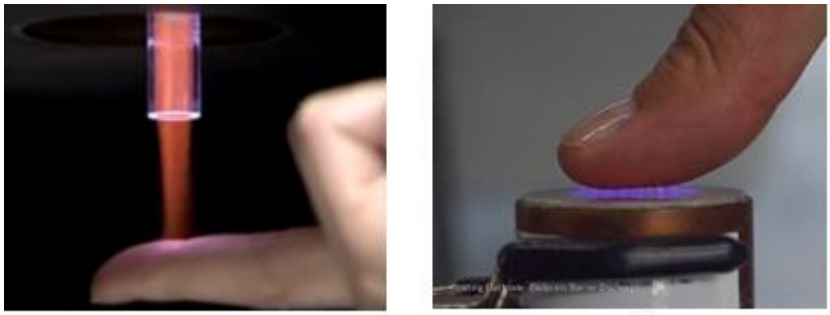

Figure 2. Picture of unharmed human skin being exposed to plasma: a) plasma torch and b) floating electrodes [28, 29].

2.1.3. Types of DBD

One of the simplest yet effective means of producing plasma is through dielectric barrier discharge (DBD). Its simple structure and flexibility raise its potency for use in industry. DBD is a method of plasma generation in which the accretion of charge on one side of a dielectric medium between two electrodes creates plasma [4]. The dielectric material acts as a buffer to prevent charge from passing through. Eventually this continues until the charge halts growth and the discharge extinguishes.

This type of plasma generation has two variations: surface DBD and volumetric DBD. Although volumetric DBD has a large amount of literature defining its traits, mainly biological uses, there are restrictions having to do with plasma gap size and inefficient use of the charged particles and UV for inactivation processes [2]. Figures 3a and 3b show that this type of DBD works by having a gap filled with a low-pressure gas between a dielectric covered electrode and the cathode. A large majority of uses for the volumetric configuration has to do with indirect exposure simply due to the nature of the structure, but research has been done to exhibit that direct exposure is significantly (on the order of a magnitude) faster than indirect [5]. Surface DBD is created through two electrodes with a layer of dielectric material between them as seen in Figure 3c. This configuration has a covered electrode and an exposed electrode. There is also an added benefit of an induced body force that this configuration creates. This is the main justification for exploring surface DBDs in this work.

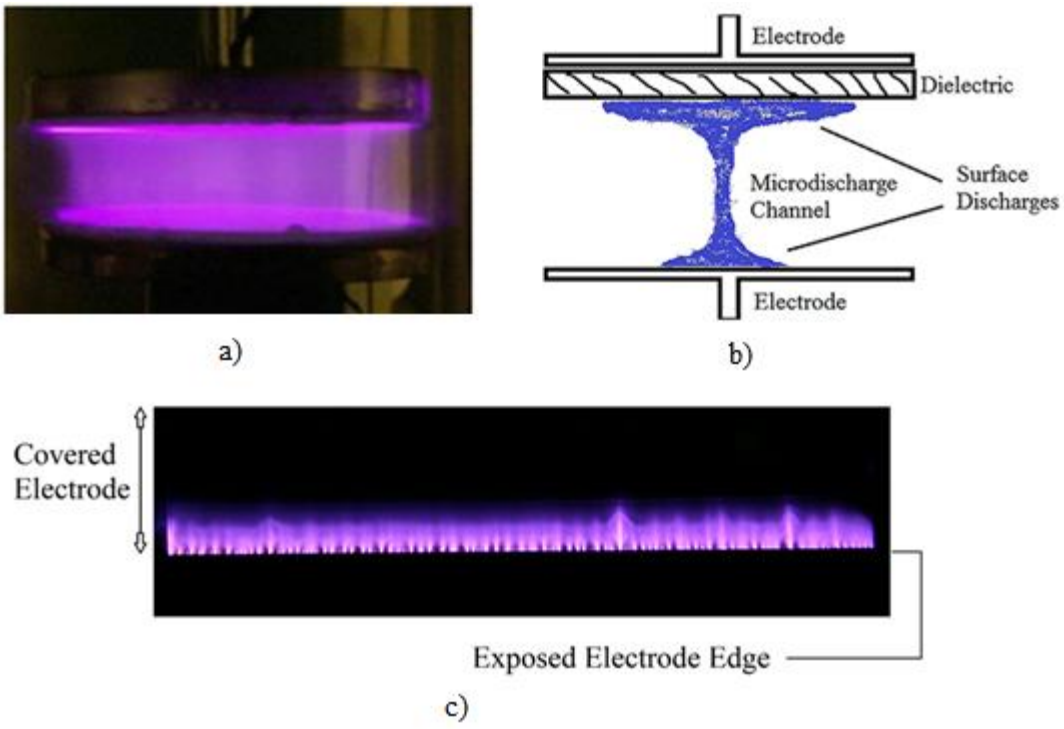

Figure 3. a) Example picture of volumetric DBD. b) Schematic of volumetric DBD. c) Example picture of a surface DBD [2].

2.1.4. Configurations of SDBD

In a surface dielectric barrier discharge (SDBD) actuator, the two electrodes can be in a symmetric or asymmetric configuration depending on the goal of the DBD actuator. The asymmetric configuration is seen in Figure 4a and the symmetric configuration is seen in Figure 4b. One side is completely covered with some type of insulation while the other side is left uncovered. This configuration works well to sustain a large-volume discharge without the discharge collapsing because of its self-limiting nature. The asymmetric configuration produces a significantly higher induced flow due to the higher total amount of plasma being formed and concentrated on one side. By having the electrode exposed for the negative half cycle of the alternating current supply, the electrode is more negative than the dielectric material along with the encapsulated electrode. Electrons are emitted and accumulate on the surface of the dielectric

material. This forms a barrier that functions as the root of the DBDs name. The accretion continues until a discharge occurs. The advantages of this configuration come in many forms. An induced body force comes from the interaction between the applied electric field and the plasma. The region of plasma can only be between the electrodes so a high voltage that causes sparking due to excess charge build-up does not pose a problem [6]. Combining several actuators can additively increase the velocity of the induced flow. The fabrication of this type of actuator is relatively easy to perform because of the flexibility from its simplistic structure and the electrodes can be positioned in specific ways that are necessary for their application.

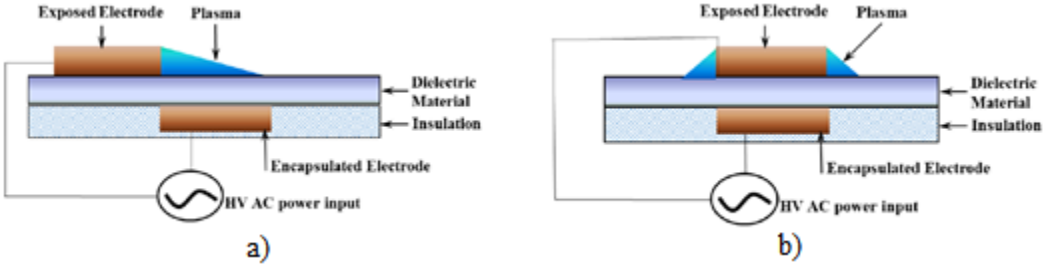

Figure 4. a) Asymmetric SDBD configuration schematic. b) Symmetric SDBD configuration schematic [2].

2.2. Induced Flow Mechanism

2.2.1. SDBD Induced Flow

In SDBDs the plasma region's electric field drives the fluid located in the vicinity adjacent to the actuator under the guise of a horizontal wall jet [32]. This pseudo wall jet has been measured up to velocities of 10 m/s a few millimeters downstream from the actuator. Due to the asymmetric configuration, the induced flow is directed away from the exposed electrode as seen in Figure 5a [4]. A suction mechanism is present directly above the exposed electrode that streamlines the flow closer to the actuator. Figure 5b demonstrates a PIV measurement of a linear actuator in quiescent flow foreshadowing upcoming results. The unidirectional flow of the induced body force has been suggested to occur due to the differences between the positive and

negative half cycles. The flow heads downstream of the exposed electrode because the plasma is more uniform and higher in volume during the negative cycle [10, 11]. The gas in the vicinity of the electric field becomes ionized due to the electron collisions. Negative ions are then propelled because of the electric field.

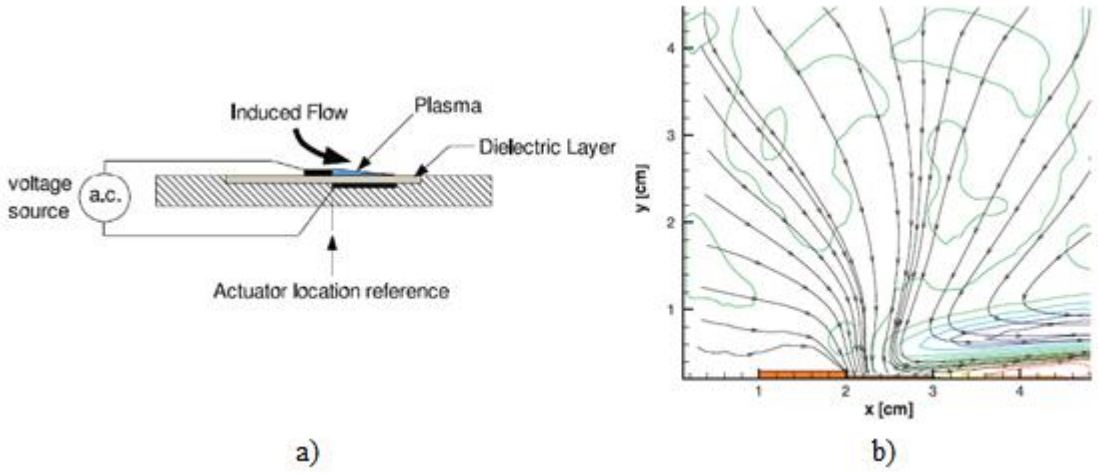

Figure 5. a) Schematic of a SDBD producing induced flow. b) Illustration of the flow field created by a SDBD's induced flow.

The flexibility of manufacturing SDBDs allow for specific geometries for exact purposes. By constructing combinations of SDBD actuators in different configurations, the strength and direction of the induced flow becomes controllable as seen in Figures 6a and 6b. Unique geometries may be used to form nozzles, or other flow directing devices.

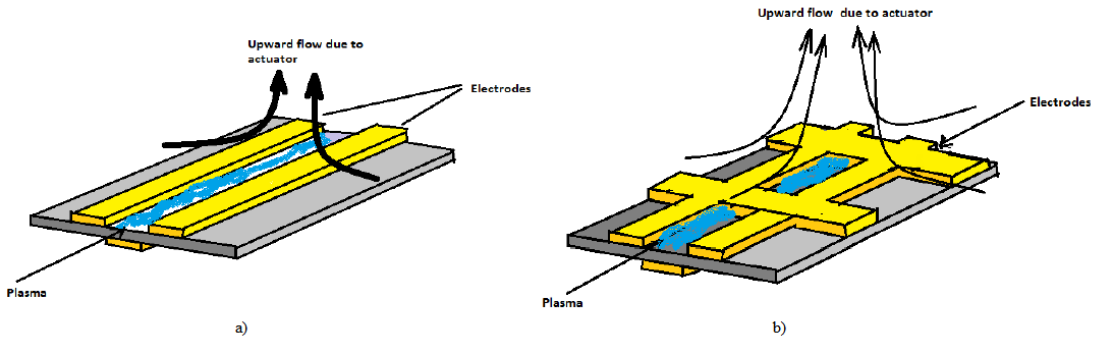

Figure 6. Example configurations of induced flow manipulation. a) Two outer electrodes and b) cross pattern electrodes [2].

Due to the force being induced by the electric field, many parameters fall into controlling its strength. Increasing the voltage and decreasing he alternating current frequency has been shown to affect the flow linearly [2]. This paper works to identify and observe various parameters that can potentially affect the induced flow through the dielectric material.

2.2.2. Body Force

The body force, F_B, observed from SDBD has been explored in-depth to the point in which a theoretical equation has been defined to estimate its value. The body force has been defined as

$$F_B = \rho \boldsymbol{E} = -\left(\frac{\varepsilon_0}{\lambda_D^2}\right) \phi \, \mathbf{E} \tag{3}$$

where ρ is the density of electrons and **E** is the electric field [34]. The Debye length that was discussed earlier is a characteristic variable in this definition. In addition to this, a more generalized equation is defined

$$F_B = f(\Delta V, e, l, d, \dots) \tag{4}$$

where the body force is defined as a function of several parameters including characteristic lengths that make up the SDBD actuator's physical dimensions [34]. Understanding this body force and how to derive it is useful for determining theoretical values of actuator outputs along with defining efficiency, which will be discussed in Chapter III.

2.2.3. Potential Uses

The induced body force created from the SDBD has the potential to be harnessed for many applications. In the case of SDBD usage as a bacteria inactivation mechanism, the induced flow can aid the delivery of the created plasma species to a sample. A stronger induced flow dictates a larger range of effectivity. Additionally, the direction may be manipulated to fit various

geometries. For SDBD mechanical usages, essentially any system using air flow potentially may be affected. SDBD actuators have appeared in the form of accelerometer arrangements that are used for measuring temporal reaction forces, as cylinder flow controllers, as noise reducers, as flow separation controllers and even as hypersonic flow controllers [19-25]. Details about some of these experiments appear in Figures 7 and Figure 8. Flow separation control especially stands out as it is directly using the induced flow to reattach separated flows thereby reducing drag.

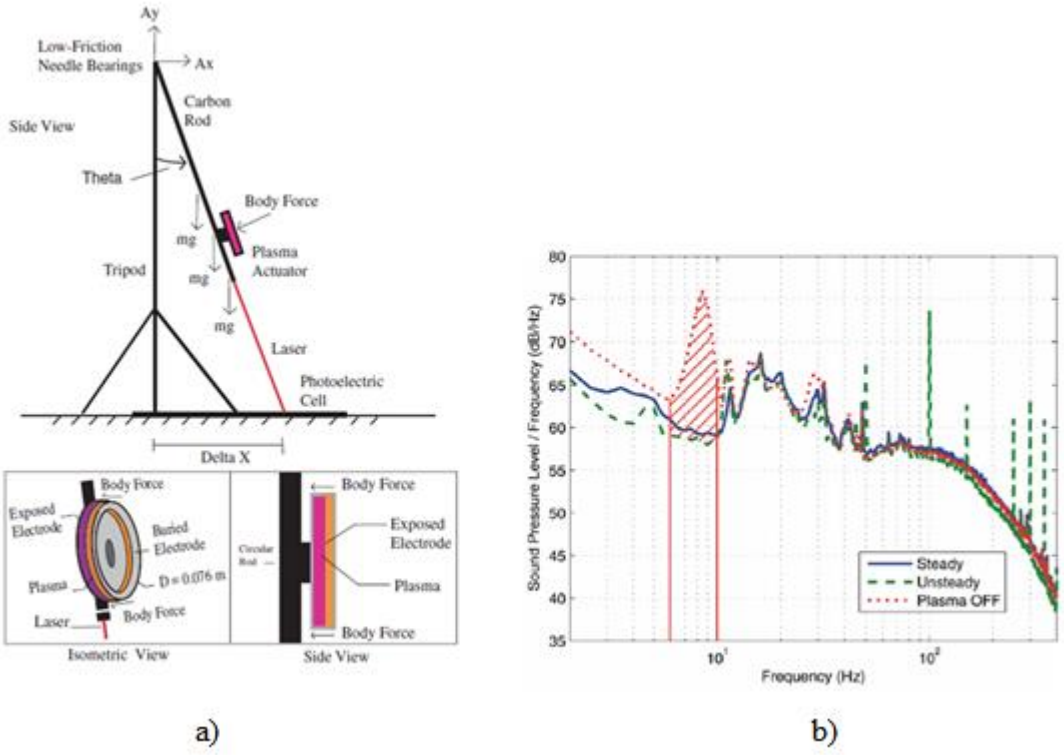

Figure 7. a) Pendulum arrangement for the reaction-force measurement that centers on a plasma actuator. b) Plasma actuation effects on near-field SPL spectra [19, 20].

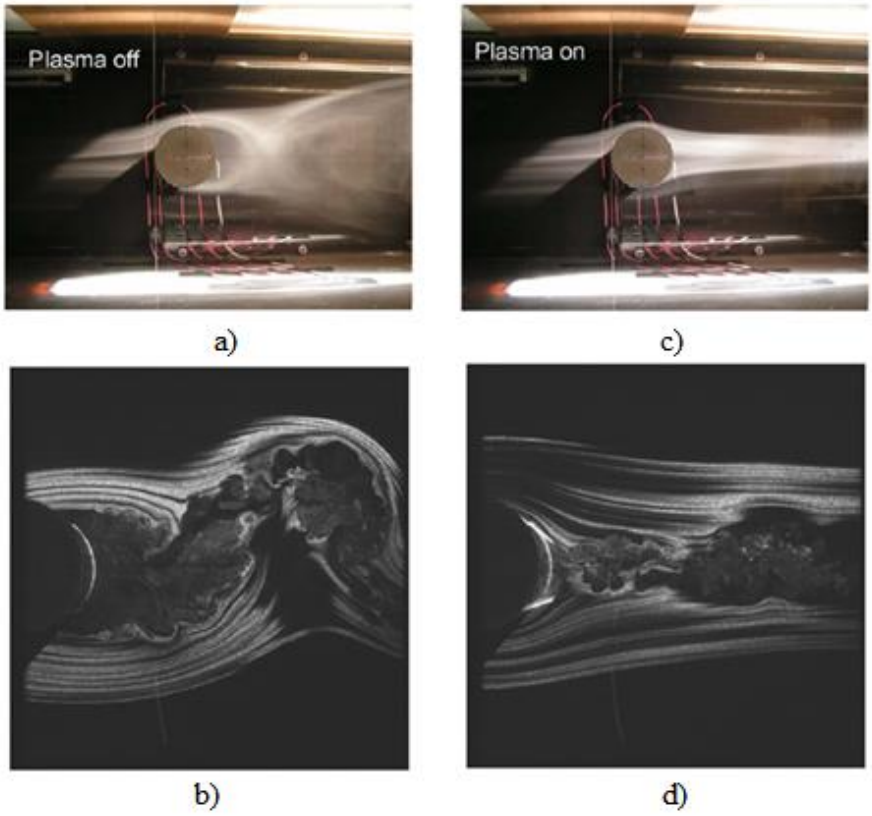

Figure 8. a) Smoke-flow visualization with actuators off. b) Near-wake PIV flow visualization with actuators off. c) Smoke-flow visualization with actuators on. d) Near-wake PIV flow visualization with actuators on [21].

Historically, the maximum value of velocity that the induced flow can produce has not been outstanding. Propulsion is a field unnoticed as an avenue of plasma research simply because the thrust produced is insignificant in comparison to the gross weight of possible aerospace systems. Additionally, the amount of voltage required to discharge the SDBD actuators is significant enough to warrant a stronger power supply. But due to the proliferation of sUAS and the sway of technology towards a smaller unit, the reality of plasma propulsion is becoming imaginable. Power supplies, like batteries, have not caught up to their technological counterparts in terms of size and efficiency but have been estimated to in the near future [33]. If the efficiency of SDBD actuators were optimized and the fabrication of small power supplies becomes an actuality, then powering a tiny system is not impossible. This idea of plasma propulsion boasts no moving parts, a quick time response, flexibility, scalability, low mass (minus the power supply), and may be made flush with the object being propelled.

CHAPTER III

SCALING

3.1. Previous Research

A key advantage of SDBD actuators is their ability to scale. The plasma itself does not scale, but the things it can affect has the ability to scale, for example, the induced body force. In most cases, changed parameters produce linear results allowing for simple manufacturing induction. There are many factors that may be scaled for a SDBD actuator. Previous research has been done to observe optical, electrical and thrust characteristics of these actuators [34]. Equation (4), although generalized, represents the ability for the body force to scale. Pai presents research on specific parameters that affect input voltage: width of the electrode, length of the electrode, and number of electrodes [3]. Those results show that the width of the electrode has no effect on the input voltage, increasing the length of the electrode increases the input voltage linearly, and increasing the number of electrodes increases the input voltage linearly as well. Understanding the input voltage sets up the understanding for optimizing induced flow. Previous efforts have studied ways to control the frequency of the plasma and the input voltage permitting them control over the production of plasma and the type of plasma produced, but less research has shown these parameters in regards to altering the induced flow. A comprehensive guide is necessary combining the preliminary research over the primary factors affecting the plasma (geometry,

frequency and voltage) and the secondary factors being affected by the plasma (induced flow and plasma species created).

3.2. Scaling Effect on Induced Flow

Building on previous works, the following three parameters were chosen to observe: dielectric constant, dielectric thickness, and electrode gap distance. There is an overall lack of testing performed on the material used as the dielectric in SDBD actuators. Pseudo "optimal" materials have been chosen due to their effectiveness in proving results, but relationships have not been fully established. The parameters of dielectric constant and thickness were chosen because of their guaranteed effects on the plasma produced and thusly their effect on the induced flow. Electrode gap distance has always been known to affect induced flow strength, but an in-depth analysis is still necessary on its relationship between the input voltage, the creation of streamers, and how these streamers affect the induced flow. The electrode gap distance parameter was chosen as a confirmation of previous results as well as an addition to boost induced flow strength. Figure 9 displays many of these physical characteristics.

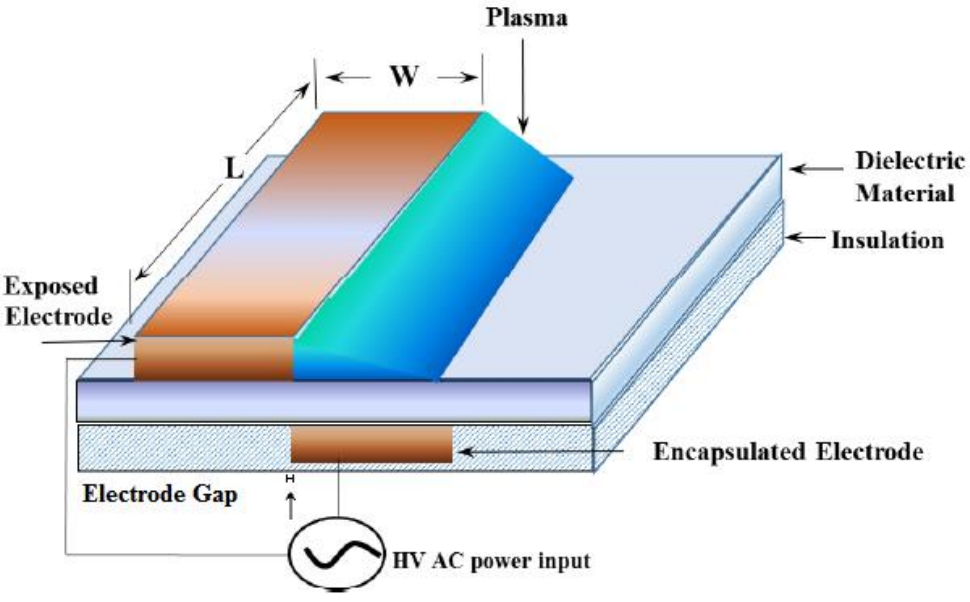

Figure 9. Schematic of SDBD displaying various geometric features including electrode gap distance, width, and length of the actuator [2].

3.2.1. Dielectric Constant

This parameter is of the highest physics point-of-view complexity between the three chosen parameters. Being a crucial member of a SDBD actuator, analysis of this material is paramount to effectively increasing its production of induced flow. Dielectric constants, also known as the relative permittivity, is a measure of the relative charge storage capabilities of a dielectric material [35]. A larger dielectric constant normally yields a greater ability to store energy. With this definition of dielectric constants it is a simple step away from drawing parallels between capacitors and DBD actuators. Corke et al. has presented various improvements in SDBD actuators by means of calculating their capacitance [1]. They use a space-time model that demonstrates the system as a parallel network of air capacitors, dielectric capacitors, plasma resistive elements and zener diodes. The air capacitance is given by Equation (5)

$$C_{an} = \frac{\varepsilon_0 \varepsilon_a A_n}{l_n} \tag{5}$$

where ε_a is the dielectric constant of air, ε_0 is the dielectric constant of free space, A_n is the cross section of the air capacitor, and l_n is the distance over the dielectric surface. Likewise, the dielectric capacitance is given by Eq. (6)

$$C_{dn} = \frac{\varepsilon_0 \varepsilon_d A_d}{l_d} \tag{6}$$

where ε_d is the dielectric constant of the dielectric material, A_d is the cross section of the dielectric capacitor, and l_d is the distance over the dielectric surface [1]. This model aids in obtaining power dissipated by the system, which in turn aids in improving efficiency. Figure 10 displays a schematic of this model on a single DBD actuator. Using this method, the capacitance of each actuator used for testing may be calculated and compared as equalized capacitors. This method also ties in the dielectric thickness. Unfortunately, however, this calculation is outside the scope of this paper and thus will be left for future work. This affects mainly the comparison between

dielectric materials, but a vague understanding may still be obtained without exact capacitive element comparisons.

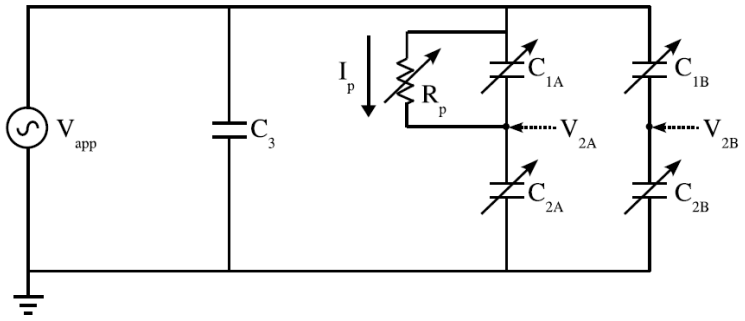

Figure 10. Schematic of the resistive and capacitive elements making up DBD [10].

Three different dielectric materials were chosen from the list in Table 1 to test. Acrylic was chosen due to its manufacturability, wide usage, and relatively low dielectric constant. Alumina was chosen because of its high dielectric constant. A glass-reinforced epoxy laminated material known as FR4, where FR stands for flame retardant, was chosen because its dielectric constant was within the range between acrylic and alumina. The comparison of results between these materials should be done with a lack of comparative capacitances in mind. Originally Teflon was chosen due to its wide usage in previous works and low dielectric constant, but circumstances delayed the arrival of said material. FR4 was then chosen as a replacement until its arrival, but after consideration, three materials was enough testing to observe general differences in dielectric constant.

Table 1. Sample list of possible dielectric materials. Highlighted sections are the chosen dielectrics for tests.

Material	Dielectric Constant
Teflon	2.1
Paper	3.0
PET	3.0
Acrylic	3.5
Kapton	3.5
FR4	4.7
Glass	7.6
Alumina	9.1

3.2.2. Dielectric Thickness

The thickness of the dielectric material has various effects on a DBD. Logic reasons that since high voltage must act across the dielectric material, a material that is excessively thick would require higher voltage for the same results. Contrary to this, a material that is marginally thin could potentially be broken through by the high voltage and thus cause the DBD to produce sparks and eventually arc. At a point of thickness ambiguously in-between these two extremes lies an optimal thickness that allows the electrons to function at a higher efficiency to induce body forces. This optimal thickness will change according to the dielectric material.

The thickness of the material also plays a part in functionality. Even if the optimal thickness to produce the strongest induced flow is determined, if the thickness is too large to realistically use for its application then it is impractical. In addition to this, the thickness of the material plays a role is altering the plasma regime. Electricity always attempts to find the path of least resistance, and due to this etching is seen to occur on plasma actuators over time. As plasma forms and the input voltage is increased, a threshold will be surpassed during discharge that can cause the actuator to produce heat or enter the streamer regime. Efficiency is not only lost but in the case of thinner dielectric materials, the actuator may become damaged. For thicker materials, higher voltage is necessary to initiate plasma generation on actuators due to the physical distance that the electrons must overcome. Once exceeded, the high voltage will produce plasma, but obtaining a uniform plasma distribution will be significantly more difficult. This requires that a large enough voltage is input so that enough electrons in the dielectric can form the plasma. The thicker the dielectric, the more voltage is required to form plasma. This relationship is logical and becomes the foundation and limiting factor for increasing thickness to improve induced flow. A plasma formation with streamers has been noted to have higher induced flow velocity.

For experimental purposes, three different thicknesses were chosen for each material. The thicknesses are denoted by T1, T2, and T3, respectively, on each actuator. In Table 2, the exact thicknesses of each actuator may be viewed. Three thicknesses allowed for a vague trend to be seen and also did not overload the total number of actuators. The thicknesses ranged between similar materials on the same sheet due to manufacturing imperfections. The range of thicknesses for the materials fell between 0.63 mm and 3.31 mm.

3.2.3. Electrode Gap Distance

Noted in many previous works, the electrode gap distance is well known for having an effect on the induced flow [36]. In Figure 12, the electrode gap distance is seen as the length between the exposed electrode and the encapsulated electrode in the electrode width axis. Using Figure 11 as a reference, an actuator created with the right end of the exposed electrode touching (if the dielectric was missing) the left end of the encapsulated electrode will be considered a gap distance of 0mm. As this value increases, the encapsulated electrode will be shifted towards the right there by increasing the distance between the electrodes. By increasing the distance between the electrodes, a higher input voltage is required to form plasma, similar to increasing thickness. In fact, increasing the gap distance may be considered effectively increasing the amount of dielectric between the electrodes. Thus, while increasing the gap distance the induced flow should be relatively stronger as well. The limiting factors here are that if the gap becomes too large, the amount of voltage necessary to actuate the SDBD would also rise to a point where applying that actuator would be meaningless. Conversely, having a negative gap distance by this definition simply falls into the categories of symmetric SDBD actuators and eventually flipping the actuator induced flow direction. Similarly to thickness, the regime changes as the gap distance increases. Streamers are expected and thus an efficiency loss. This is combated by potential efficiency gain in the form of higher induced flow.

The gap distances that were chosen were 0.0 mm, 1.0 mm, 2.0 mm (±0.1). The 0.0 mm was the base case used as the standard for thickness testing as well. The 2.0 mm was a large separation that acted as the extreme case. These gap distances were denoted on the actuators as G1, G2, and G3. Together with the thicknesses, actuators were named with their thicknesses first followed by their gap distance. For example, an acrylic actuator with the smallest thickness and a base case gap size would be named "AcrylicT1G1." All actuator cases are presented in Table 2.

Table 2. List of all actuators created. T# represents thickness changes and G# represents gap distance changes.

Material Type	Actuator Type	Thickness (mm) (±0.1)
Acrylic	T1 G1	1.81
	T1 G2	1.75
	T1 G3	1.59
	T2 G1	1.90
	T2 G2	1.88
	T2 G3	1.93
	T3 G1	2.92
	T3 G2	3.00
	T3 G3	3.12
FR4	T1 G1	0.96
	T2 G1	1.58
	T3 G1	3.31
Alumina	T1 G1	0.63
	T1 G2	0.63
	T1 G3	0.63
	T2 G1	1.04
	T2 G2	1.04
	T2 G3	1.04
	T3 G1	3.28
	T3 G2	3.28
	T3 G3	3.28

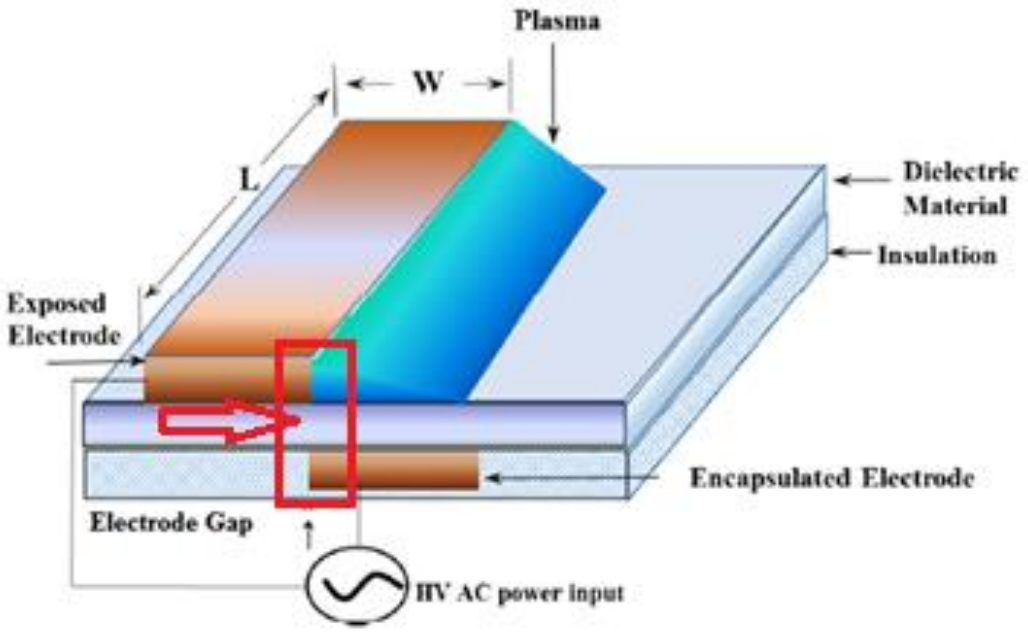

Figure 11. Repeat of earlier schematic to display specifically electrode gap distance [2].

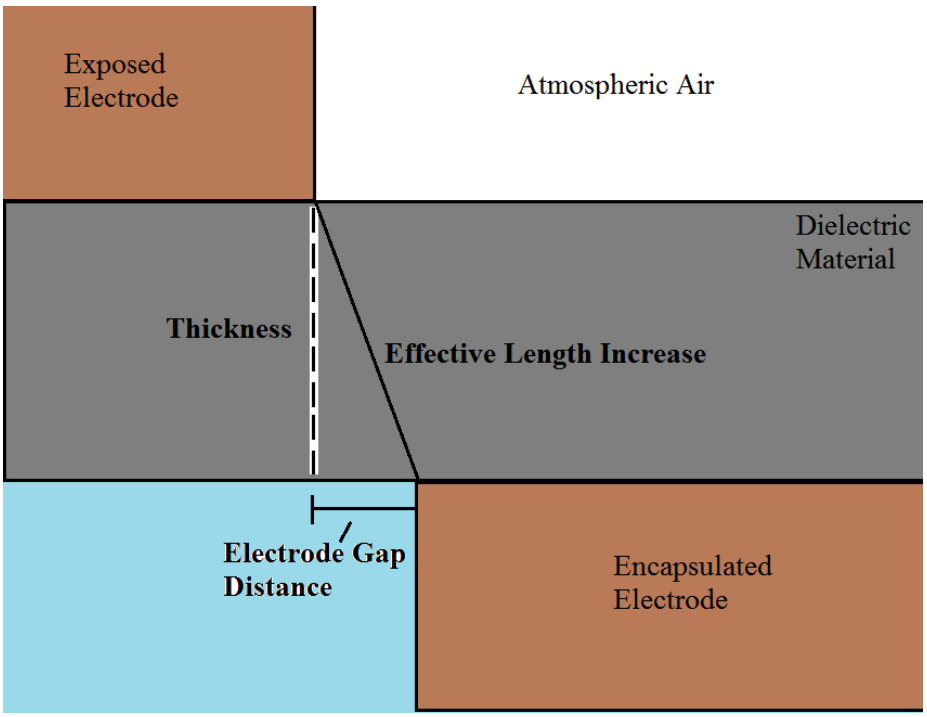

Figure 12. Illustration to explain the effective length increase from both thickness and electrode gap distance increase.

3.3. Efficiency

Improvement in efficiency is less impactful if the consequential tradeoffs are not taken into account. To improve the induced flow that SDBD actuators produce, a definition of efficiency is in order. Efficiency is normally defined as a ratio between power output and power input. This proportion displays how effective the subject is at using the energy it is given. The actuator input may be defined as a function of the input current and input voltage. The actuator output is defined by Enloe as the induced body force, which is based on the induced flows velocity [34]. The body force itself is defined as a function of the potential, various parameters from electrons, and several geometric parameters. This body force is a complicated term that has numerous parameters. By utilizing this body force and calculating the volumetric flux that is created by the body force, a calculation of momentum transferred can be obtained. In the overall scope of proving plasma's viability as a propulsion mechanism a calculation of efficiency is necessary, but in the scope of this paper only the direction of calculation is given. A comprehensive guide on proportionality between the three parameters given above and their effect on the efficiency of an actuator is potentially the final level of this research. The general equation for efficiency is defined as

$$\eta = \frac{P_{out}}{P_{in}} = \frac{P_{out}}{VI} = \frac{W/t}{VI} = \frac{Fv}{VI} \tag{7}$$

where F is the induced body force, v is the velocity of the induced flow, and VI is the input power downstream of the transformer. Plasma actuators are historically known for having low efficiency (lower than 5%), but this work is performed in an attempt to increase this value. This work will not calculate the efficiency, but outlines it for future work.

3.4. Actuator Parameters

In order to observe the changes in induced flow due to the changes in the parameters above, various factors must be held constant while others must be varied one by one. In all experiments and test cases that appear in the following two chapters, all actuator electrodes are made using commercial copper tape 6.5 mm in width. The electrode lengths for each actuator were approximately 75 mm. All actuators were made in standard configuration of a single asymmetric surface dielectric barrier discharge actuator as seen in Figure 11. Figure 13 displays the differences between the actuators.

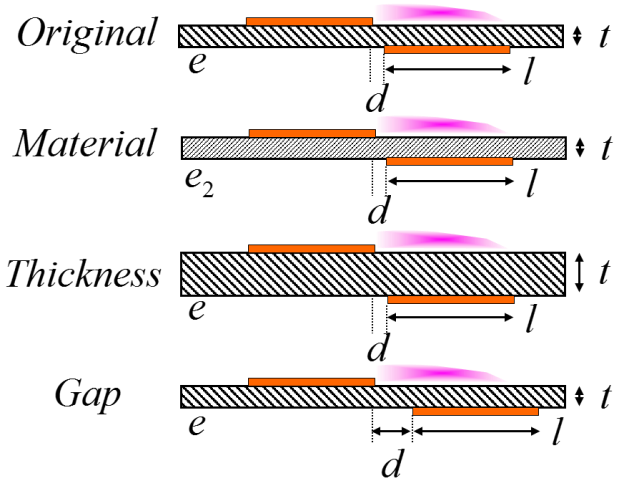

Figure 13. Schematics of difference test conditions: change in material, thickness, and gap distance.

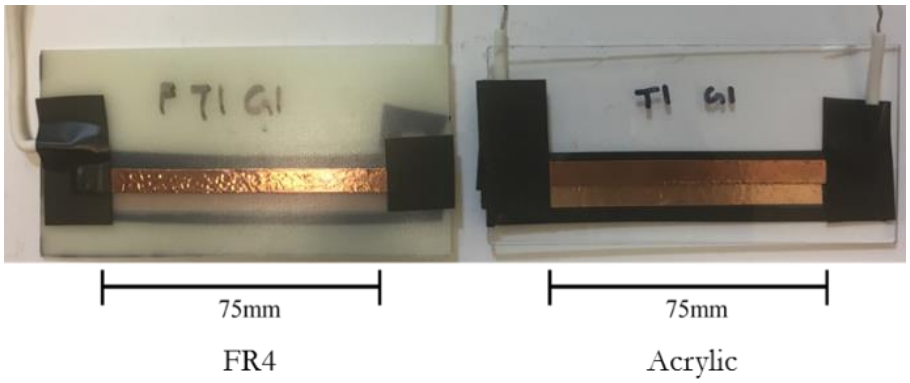

Figure 14. Picture of handmade actuators. Left: FR4, Right: Acrylic. This picture is taken post-testing.

3.5. Limiting Conditions

The power supply used was a CSI12001X DC regulated power supply that ran 1-120 V with an inherent cap of 1.00 A. Due to this cap, a current benchmark of 0.80A was set as maximum current output. The power supply could not actuate the AluminaT3 series of actuators because of the combination of the physically large thickness and the high dielectric constant. Thus, some of the tests for this actuator proved inconclusive. The transformer used was an Information Unlimited MINMAX70 that runs at 7 kV and 10 ma. The transformers output is at a frequency between 25 to 35 kHz. The thicknesses of the materials were off-the-shelf and no machining was done to shave off thicknesses meaning there were irregularities within the thicknesses. The tolerance here are approximately ±0.13 for acrylic, but ±0.00 for FR4 and alumina. Only one actuator was made for each specific type of actuator, so as actuators were tested and then retested, the results changed due to the pitting and wear on the actuators.

CHAPTER IV

OPTICAL IMAGE ANALYSIS

4.1. Background

With the combined technology of high resolution digital cameras with powerful image processing programs, a different way to analyze plasma has arrived within the past decade. Previous works have shown that optical emission spectroscopy (OES) may work for observing plasma species and uniformity [2]. But to simply view the plasma and ensure its uniformity (or how close it is to uniformity) is difficult to do with the naked eye. Optical image analysis is a simple method to place a quantitative, albeit arbitrary, value to the plasma actuator emission. It not only allows for quick assurance that plasma is uniform, but also can act as a means to compare plasma regimes across different instances. Optical image analysis is vague and general name, but in this scenario it denotes a process of camera image pixel intensity breakdown. By transforming an image into its grey scale form, the intensities may be matched and compared to the area around it. This method requires that the only pixel source be the emitted plasma, but in doing so, intensities may be viewed. Uniform and streamer regimes may be compared using this method along with the growth and evolutions into one another. Additionally, un-grey-scaled images may be analyzed to understand what plasma species are being created by that specific configuration. This is currently out of the scope of this work due to the color complexity.

4.2. Previous Work

Figure 15 displays a plot from an optical emission spectroscopy analysis that was previously done. Various plasma species can be identified using this. By observing how these species change, a correlation to plasma uniformity could be drawn. In a previous work by Rojas, different means of characterizing plasma actuators was discussed such as simple optical measurements. Schlieren and shadowgraphs were mentioned as possible means of visualizing the induced flow field produced by these actuators as well [14]. Various derived quantities were calculated and plotted as seen in Figures 16a and 16b.

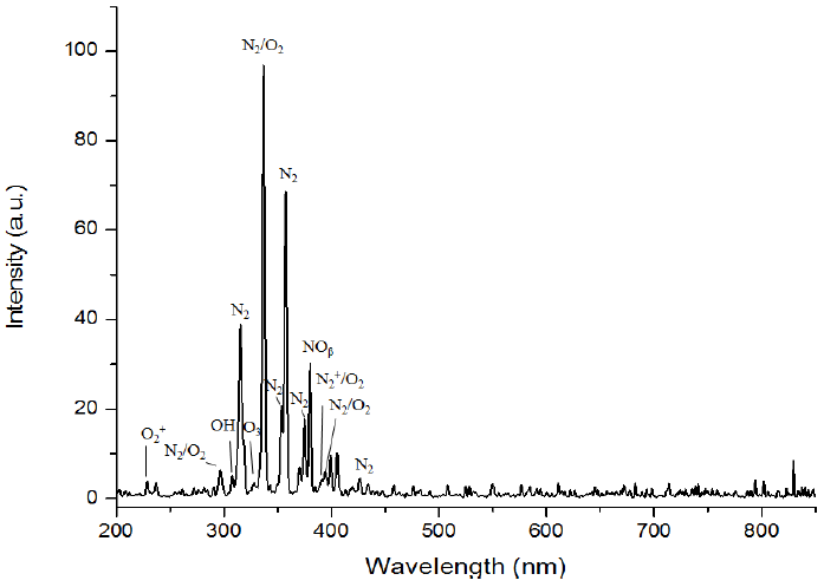

Figure 15. Optical emission spectroscopy results for atmospheric pressure surface dielectric barrier [2].

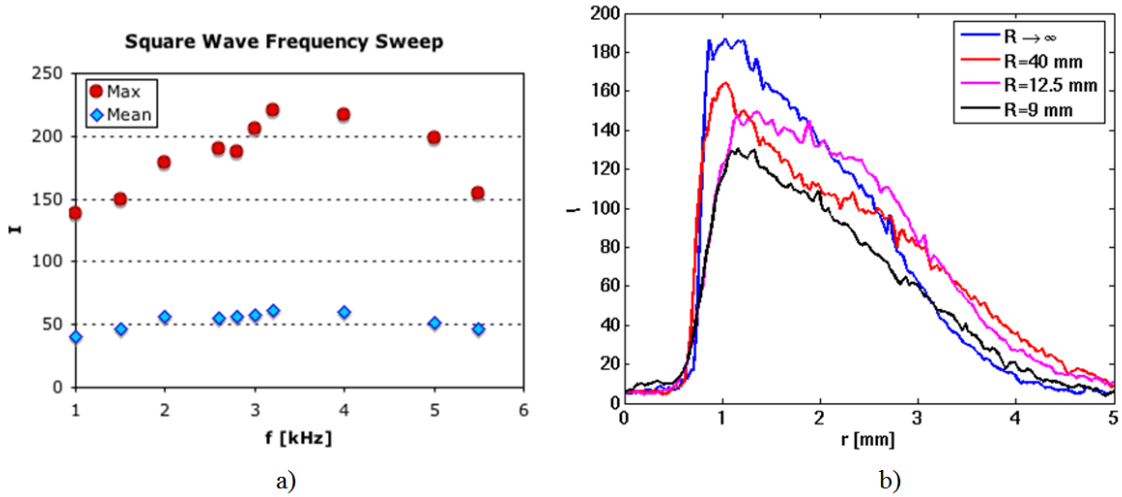

Figure 16. a) Plot of maximum intensity values tracking plasma strength across frequencies. b) Plot of curvature effects. Conductor side gradient decreased while downstream side spreads out [14].

4.3. Experimental Setup

4.3.1. Apparatus Setup and Software Settings

Figure 17a displays a schematic of the setup for this experiment. The camera used for taking the images a Canon Digital Rebel XTi. This camera was chosen due to its simplicity. The focus and exposure were all completely manually controlled. A CSI12001X DC regulated power supply was used in conjunction with a custom transformer from Information Unlimited (7 kV and 10 mA) to power the actuator. The camera was mounted to an optics bench and the actuator was strapped in place to ensure similar images. The camera was mounted approximately 150 mm away from the actuator.

Several exposure times were tested to see which provided the best image pre-processing quality. An optimal amount of lighting existed to properly distinguish between uniformity and non-uniformity, but not so much that the camera images became oversaturated. In Figure 17b, three examples of exposures (2 s, 5 s, and 10 s) each used the same actuator at the same current benchmark (0.50 A). The actuator is an acrylicT3G1 which theoretically would provide a

decently uniform plasma distribution. The similarities between the images is obvious, but there are distinct details being lost in each example. The longest level of exposure shows an example of oversaturation. Too much light has been accumulated and details are lost in the radiance of the actuator. The shortest level of exposure does not have nearly as much detail and fails to distinguish itself from others taken at that exposure. Thus, 5 s of exposure time was chosen as a medium between the two.

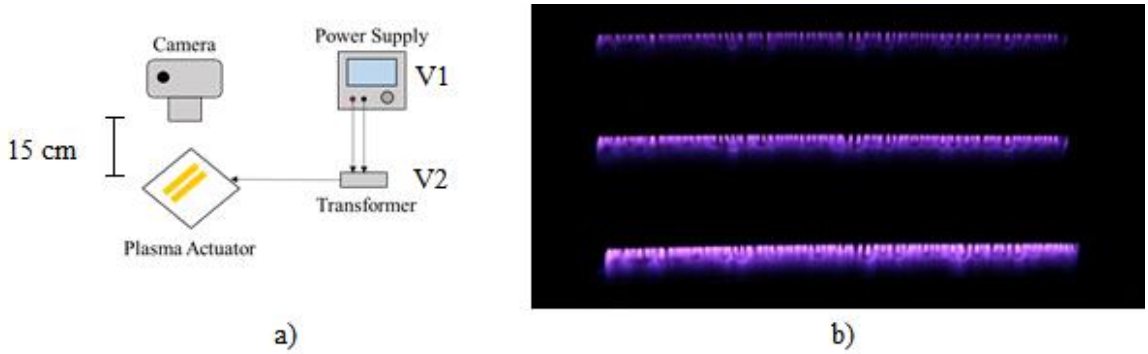

Figure 17. Schematic of OIA setup. b) Exposure time sample mages: top is 2", middle is 5", and bottom is 10".

The images are run through a MATLAB program specifically created for grey scale conversion, intensity calculation, and graph development using the attained information. This program is viewed in the Appendix. An average intensity of each pixel of plasma across the width of the actuator was compared to its respective length position. This allowed for a more quantitative measure of plasma uniformity for comparison over simply judging with the naked eye. The main idea behind this program is to observe specifically when the plasma becomes "uniform" or at least set a point at which this can be categorized as such.

Specifically, the program converts the image into a greyscale with arbitrary but consistently comparable intensity values, averages all the intensity values in the y-direction for a specific x-location on an actuator, and plots this versus the average intensity value's x-coordinate. It is easiest if an almost completely black image other than the plasma to ensure only the plasma

is being averaged. Additionally, the images needs to be oriented so that the streamers will be along the y-axis and the length of the actuator is in the x-axis. This displays an interesting plot that could potentially be useful in determining the uniformity of plasma regimes. Spikes indicate streamers in that they have no other plasma lines associated with them and many spikes together begin to signify uniformity. Unfortunately, a completely uniform plasma does not exist in this method. Even in the most uniform of cases, there will be cuts within the plasma due to deformities and imperfections in the copper tape used as the electrode and the breakdown of the dielectric material being used as the buffer.

4.3.2. Testing Procedures

A 5 s exposure image is taken for each actuator at several current benchmarks. Starting with the current at which the plasma ignites, the images are taken at every rounded 0.10 A after that point igniting at 0.27 leads to 0.30 A, 0.40 A, 0.50 A and so forth until 0.80 A is attained. Each image is then sent through the MATLAB program and each resulting plot is categorized with its specific actuator.

4.4. Analysis of Optical image Analysis

Table 3 displays the voltages that the actuators required to hold a current of 0.80 A. The voltage values would slowly change over time as the actuator remained on because of the wear on the dielectric. The plasma requires more power because the resistance increases due to the wear causing the current to overcome the increase. Additionally, for each set of actuators tested, the optical image plots belonging to that actuator stands immediately before the discussions.

Table 3. List of DC input voltages required to maintain the actuator at a current of 0.80 A.

Material Type	Actuator Type	DC Input (V_1)
Acrylic	T1 G1	26.0
	T1 G2	26.0
	T1 G3	25.3
	T2 G1	27.0
	T2 G2	26.7
	T2 G3	27.0
	T3 G1	28.9
	T3 G2	29.7
	T3 G3	30.0
FR4	T1 G1	19.5
	T2 G1	23.5
	T3 G1	29.2
Alumina	T1 G1	15.7
	T1 G2	15.9
	T1 G3	16.8
	T2 G1	18.2
	T2 G2	18.6
	T2 G3	19.0
	T3 G1	16.0
	T3 G2	17.5
	T3 G3	19.0

4.4.1. Dielectric Constant

There are three main actuators to observe here: Acrylic/FR4/Alumina T1G1. This reduces the total number of changes while maintaining the main variable difference.

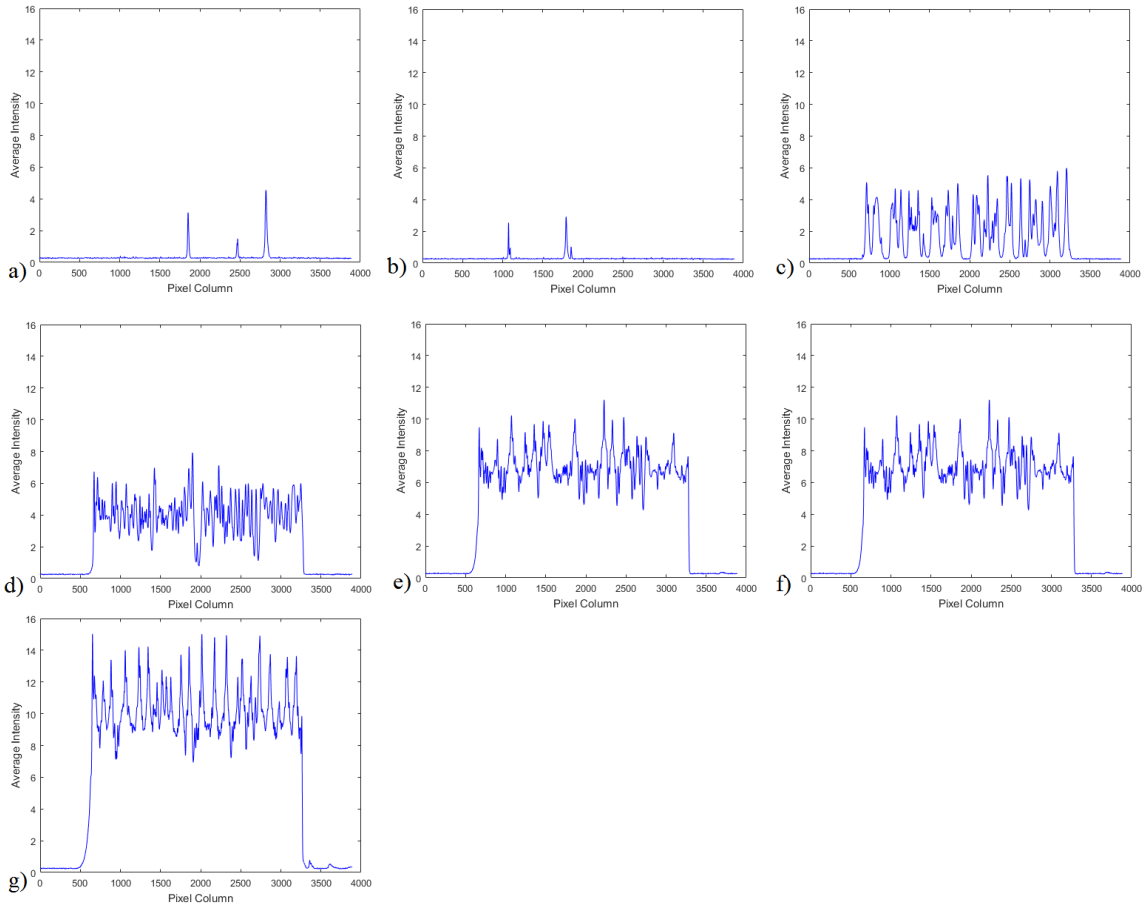

Figure 18. Intensity vs actuator length plots. a) 0.27A, b) 0.30 A, c) 0.40 A, d) 0.60 A, f) 0.70 A, and g) 0.80 A.

(i) Acrylic T1G1: With an ignition of plasma at around 11.0 V and 0.27 A, analyzed images were taken at every 0.10 A up to 0.80 A. As the voltage increases, various sections of the actuator begin to ignite eventually filling up the entire surface. The actuator becomes noticeably more uniform upon reaching 0.60 A, and when reaching 0.80 A would be easily qualified as completely uniform.

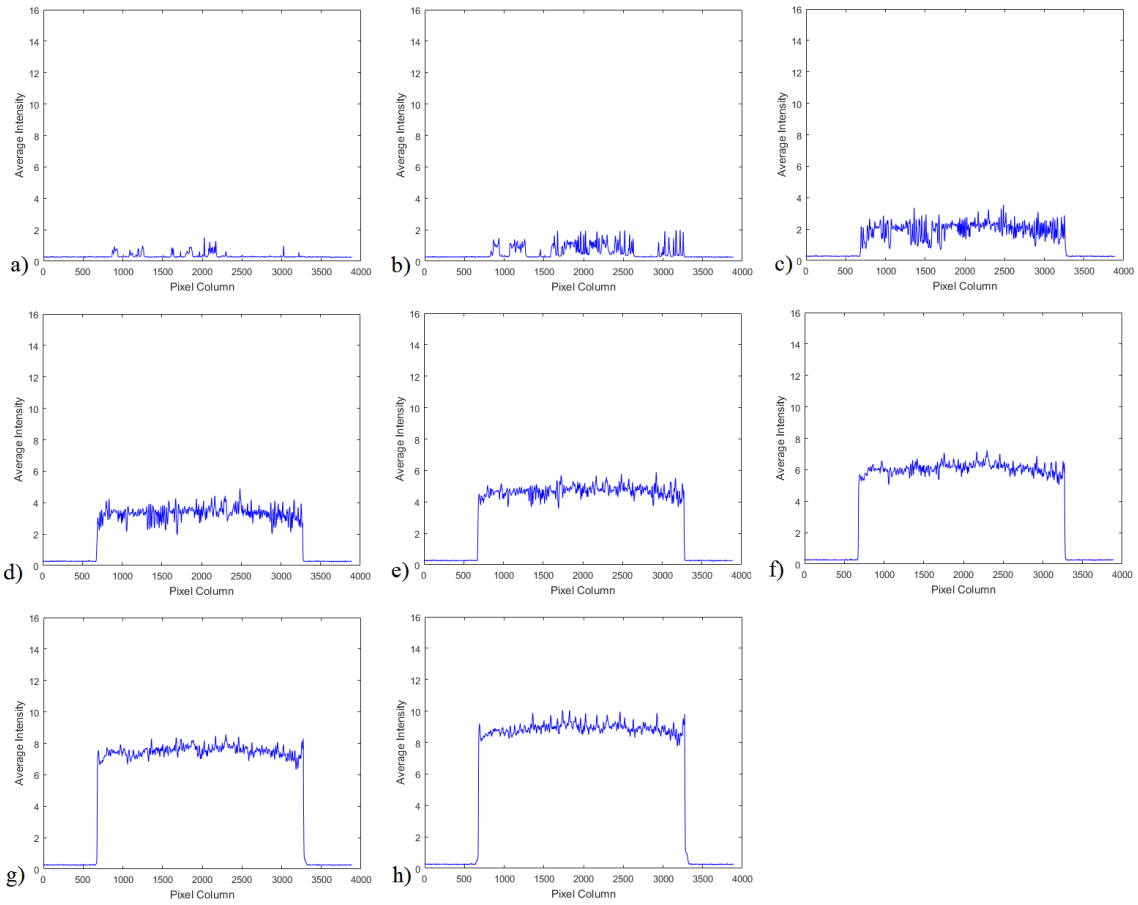

Figure 19. Intensity vs actuator length plots. a) 0.17 A, b) 0.20 A, c) 0.30 A, d) 0.40 A, e) 0.50 A, f) 0.60 A, g) 0.70 A, and h) 0.80 A.

(ii) FR4 T1G1: Igniting at 6.9 V and 0.17 A, FR4 begins its plasma regime significantly earlier than acrylic. With analyzed images every 0.10 A up to 0.80 A, it can be easily seen that uniformity takes place early on. The uniformity takes place with almost half of what acrylic's intensity was: 4-5. But rather than increasing the amount of streamers with increased voltage, FR4 seems to solidify its uniform state. Upon reaching 0.80 A, the actuator remains stable and emits a constant array of intensity as seen in Figure 20. There are few areas that would count as streamers, with an average intensity lower than acrylics at this current level.

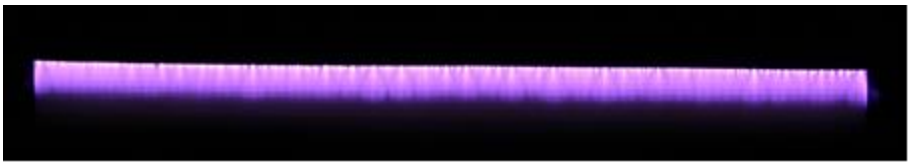

Figure 20. FR4T1G1 at 0.80 A displaying a high level of plasma uniformity.

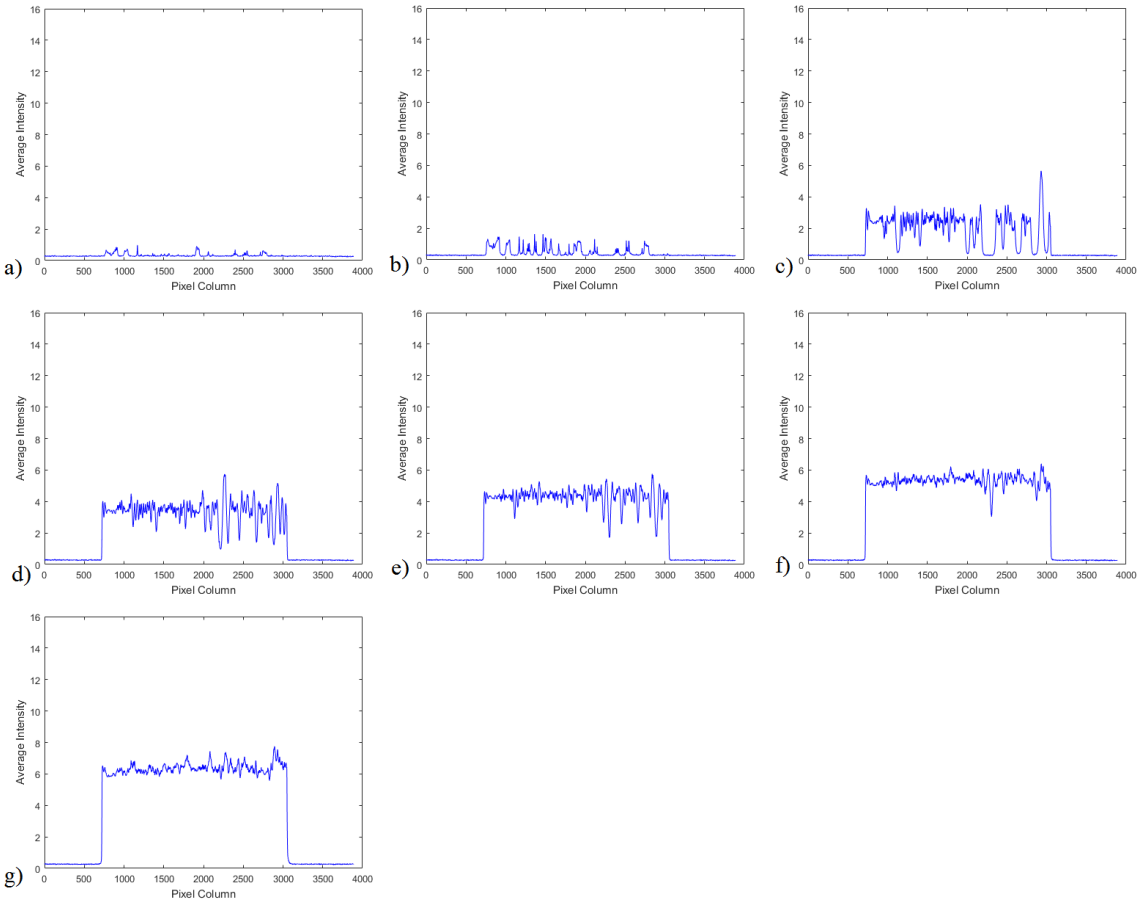

Figure 21. Intensity vs actuator length plots. a) 0.25 A, b) 0.30 A, c) 0.40 A, d) 0.50 A, e) 0.60 A, f) 0.70 A, and g) 0.80 A.

(iii) Alumina T1G1: Alumina ignites at 6.7 V and 0.25 A. Similar voltage to FR4, but with higher current. The overall intensity is noticeably lower, but the trend remains similar to that of FR4. There are not many streamers that form with uniformity completely taking over upon reaching 0.80 A as seen in Figure 22.

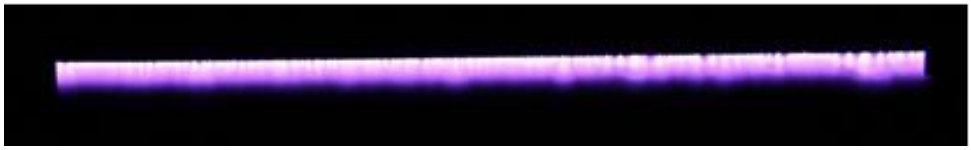

Figure 22. AluminaT1G1 at 0.80 A displaying a high level of plasma uniformity.

Overall analysis of dielectric type differences: Even though alumina has a significantly higher dielectric constant than FR4 (which is relatively similar to acrylic), they have similar trends to their plasma regime. Although not concrete, there appears to be a trend between increasing dielectric constant and a higher uniformity in plasma/weaker plasma intensity. Coincidentally, the physical thicknesses of the FR4 and alumina actuators in this case were similar while acrylic was slightly thicker.

4.4.2. Dielectric Thickness

The actuators to observe here will be the Acrylic T1G1, T2G1, and T3G1 series.

(i) Acrylic T1G1: As seen above.

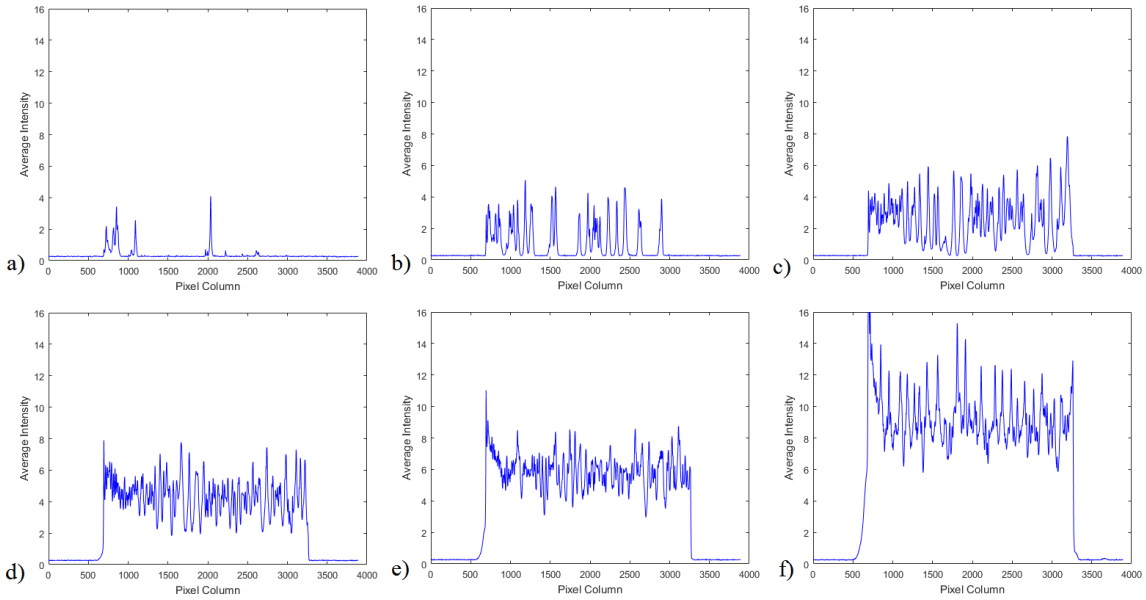

Figure 23. Intensity vs actuator length plots. a) 0.26 A, b) 0.30 A, c) 0.40 A, d) 0.60 A, e) 0.70 A, and f) 0.80 A.

(ii) Acrylic T2G1: The first thing to mention is that the large peaks on the edges should be viewed with caution because they are caused by the connections between the high voltage wires and the copper tape. This incidentally adds intensity to the edges causing them to be inaccurate. The next thing to note is that the change in thickness between acrylic actuators T1G1 and T2G1 is merely 0.10-0.20 mm (±0.13 mm). The ignition voltage and current for this actuator was 13.3 V and 0.26 A respectively. The results here are similar to the T1G1 case in all trends but the overall voltage levels seem higher with lower current.

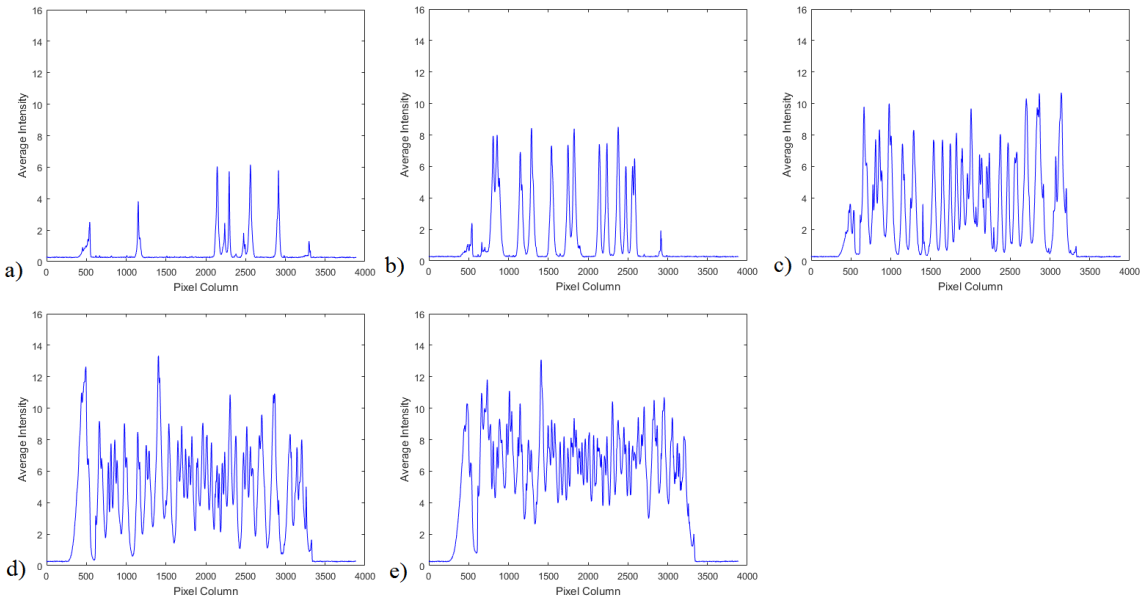

Figure 24. Intensity vs actuator length plots. a) 0.42 A, b) 0.50 A, c) 0.60 A, d) 0.70 A, and e) 0.80 A.

Acrylic T3G1: Ignition of plasma is at 20.2 V and 0.42 A. The obvious difference here is that the amount of streamers has increase significantly. Uniformity does not exist as much here with many peaks and valleys being present. The amount of current necessary for ignition is significantly higher but this also increases the initial intensity of the plasma. Final intensities are about the same as the previous cases.

Overall analysis of dielectric thickness differences: Due to the first two cases being relatively close in thicknesses not many conclusions may be drawn there. The difference between

those two and the third case is significant however. This opens a threshold of thickness in which the regime of the plasma changes drastically from majority uniform plasma to majority streamer plasma. Additionally, the introduction of streamers increases the overall amount of voltage necessary to maintain them. This test yields relatively inconclusive results.

4.4.3. Electrode Gap Distance

The actuators to observe here are the Acrylic T1G1, T1G2, and T1G3 series.

(i) Acrylic T1G1: As seen above.

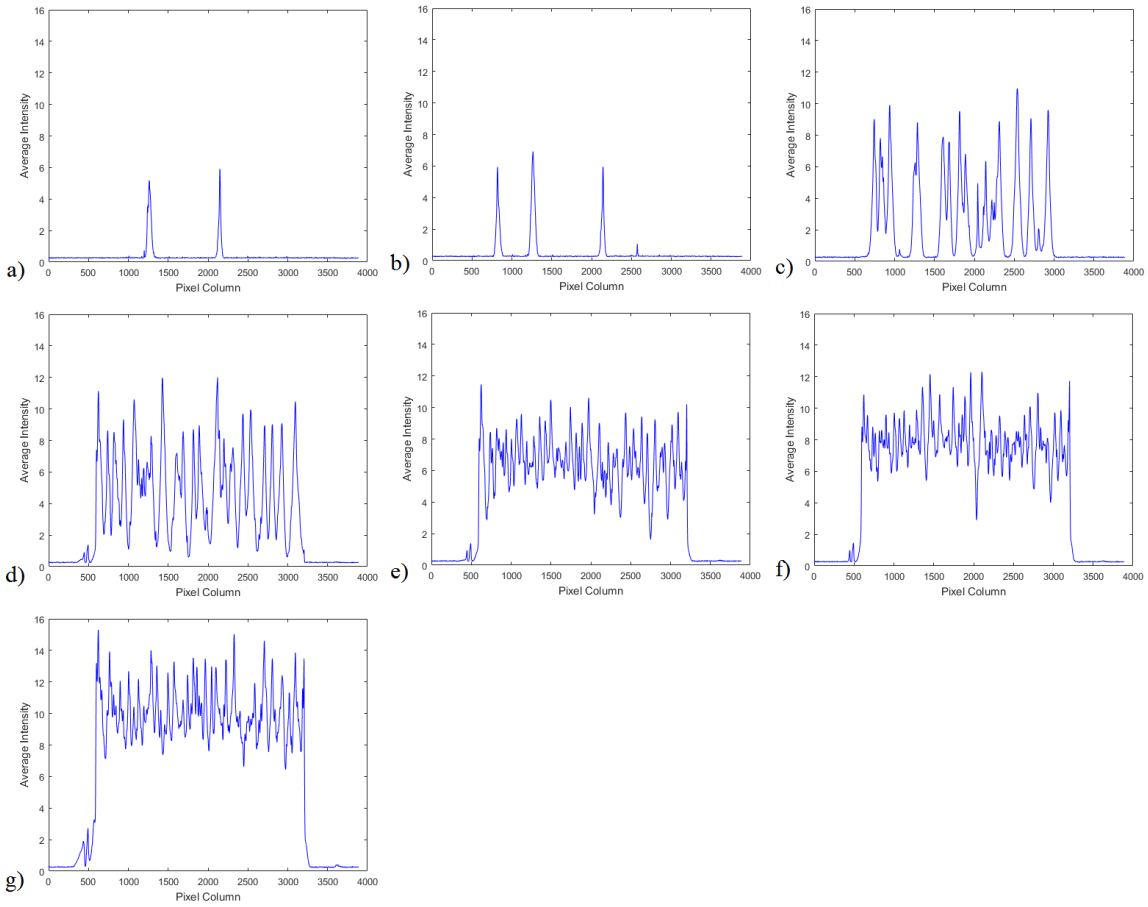

Figure 25. Intensity vs actuator length plots. a) 0.29 A, b) 0.30 A, c) 0.40 A, d) 0.50 A, e) 0.60 A, f) 0.70 A, and g) 0.80 A.

(ii) Acrylic T1G2: Ignitions points are 15.9 V and 0.29 A. Immediately upon increasing the gap distance from 0.0mm to 1.0mm, streamers begin forming immediately. At 0.50 A, it is apparent that the streamer onset has been brought forth tremendously. It is not merely just the plasma not having fully form yet. The intensity of the plasma at the location of the streamers are already at the same level as 0.80A from the previous case, approximately 10 units. Interestingly though, as the voltage increases, the streamers are leveled out and the plasma becomes closer and closer to a uniform state. Between 0.70A and 0.80A, there is only an increase in amplitude of the streamers with uniformity already taken place.

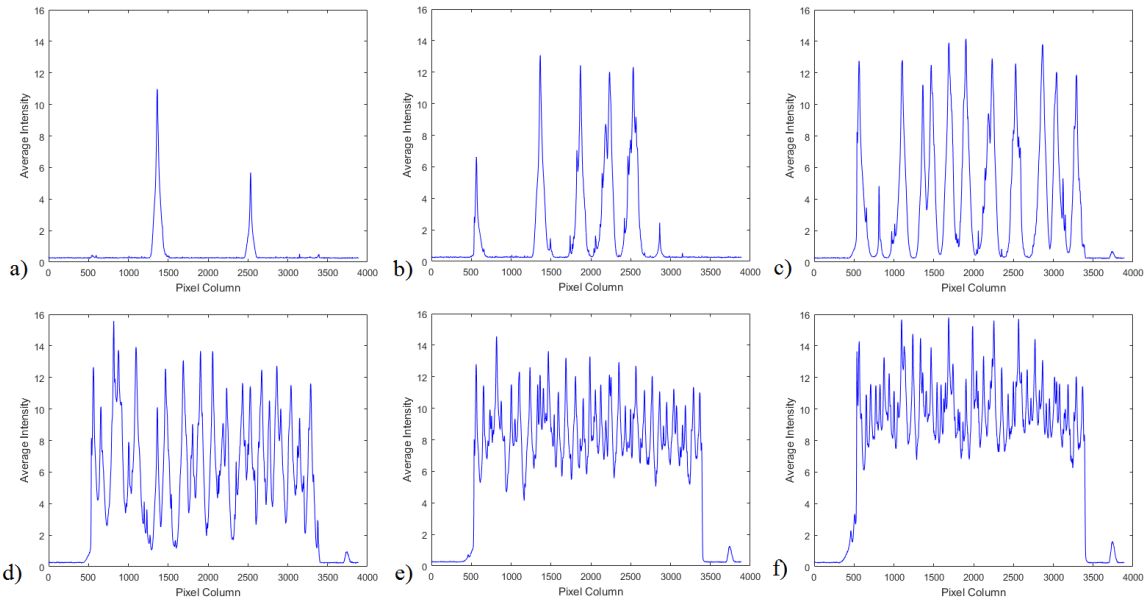

Figure 26. Intensity vs actuator length plots. a) 0.34 A, b) 0.40 A, c) 0.50 A, d) 0.60 A, e) 0.70 A, and f) 0.80 A.

(iii) Acrylic T1G3: Ignition values are 18.7 V and 0.34 A. The tiny peak on the right side of some images is the materialization of the connection between the high voltage wires and the copper tape in the intensity plot. This actuator begins with streamer onset even more so than the previous cases. By changing the electrode gap distance from 1.0 mm to 2.0 mm (±0.1 mm), the streamers become distinct and bright as seen in Figure 27. Upon reaching a certain level of current, about 0.70 A, the plasma finally begins to fully form in regions in between the streamers and approach a uniform-like state.

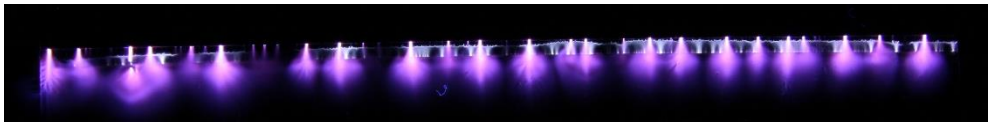

Figure 27. AcrylicT1G3 at 0.80 A displaying a completely streamer regime.

Overall analysis of electrode gap distance differences: It is clear from these three cases that increasing the electrode gap distance brings forth the onset of streamers. This is due to the increased distance that the electrons must move. Upon finding a pathway, they continuously run through it because the previous electrons have carved a lesser path of least resistance. Eventually at higher voltages, all of the pathways are used, but only after several streamers have burned significant grooves into the actuator. Uniformity happens but only towards the later stages.

4.5. Derived Quantities

Certain information may be obtained by observing the OIA plots closer. By integrating the intensity versus pixel column equation, the area under the curve is obtained which represents the total amount of plasma. For example, looking at the acrylicT1G1 actuator operating at 0.80 A yields the orange curve in Figure 28. In addition to this, the area at specific points of the actuator length may be plotted against its respective position to obtain a slope that represents the uniformity of plasma across the length of the actuator. This is displayed as the blue curve in Figure 28. The area vs. length curve regularly displays a linear curve unless the resolution of data points is increased to maximum. The slope itself represents the degree of plasma generation, as in a higher positive slope indicates more plasma being created. In Table 4, each actuator has its representative plasma area. Looking at gap distance increase from acrylic, there is not a large variation in plasma generation. Additionally, increasing thickness seems to have the effect of lowering the area, which can be seen visually as well. Altering materials also seems to have a significant effect on plasma generation (higher dielectric lowers plasma area). This is due to the higher dielectric material not quite reaching its potential. As seen in the above OIA section, the acrylic has reached its streamer regime causing some of the plasma to release its energy in the

form of heat. The FR4 and alumina cases have yet to fully shift into their streamer phases and thus are still efficiency using their energy to produce a uniform plasma (as is indicated by the slopes from their area vs. length plots as well). Observing the area provides a secondary check and a quantity to the observations seen at the beginning of Chapter IV.

Finally, a standard deviation was calculated for each actuator to determine its uniformity. The limits were taken from the beginning of the plasma and across the length to the end. Table 4 also displays the standard deviations. Note that FR4 and alumina are the lowest with only 0.32 and 0.34 respectively. All acrylic values were between 1.49-1.81. This correlates with what was visually observed by the OIA raw images.

Table 4. List of actuators used in OIA and their respective area (plasma representations) and standard deviations (uniformity representations).

Actuator Type	Area	Standard Deviation
AcrylicT1G1	27500	1.49
AcrylicT1G2	27000	1.52
AcrylicT1G3	29000	1.78
AcrylicT2G1	24500	1.63
AcrylicT3G1	20000	1.81
AluminaT1G1	15000	0.34
FR4T1G1	23500	0.32

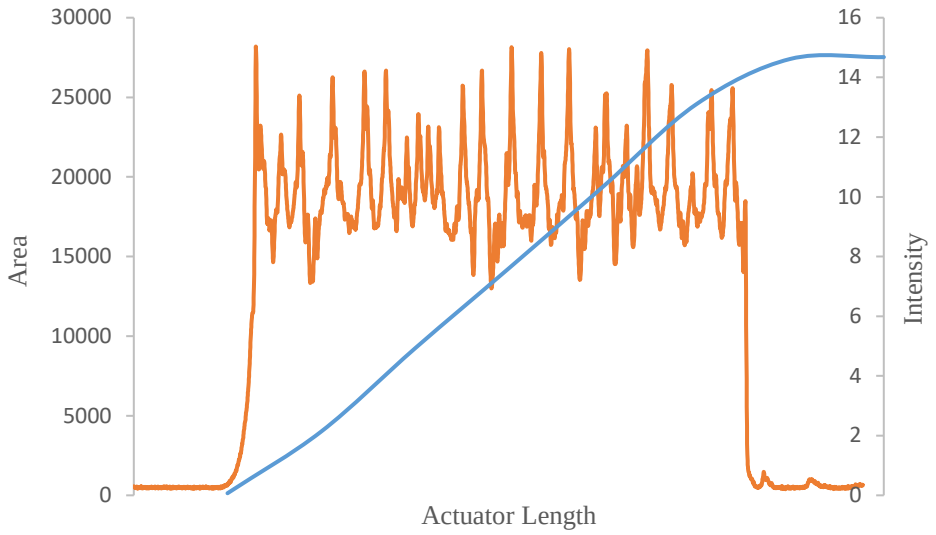

Figure 28. AcrylicT1G1: Double vertical axes plot of intensity versus actuator length at 0.80 A and area versus actuator length.

4.6 Overall Analysis of Optical Image Analysis

Optical image analysis seems to function well as a quick and dirty alternative to quantifying plasma uniformity. The accuracy of using light intensity as plasma intensity proves to be strong. The downside stems from requiring a completely black image other than the plasma which causes various forms of errors to take place light from the connections. The utter simplicity of this method makes it viable as a reliable check for our eyes, but this method does not demonstrate any knowledge of the plasma species themselves. Additionally, the resolution of the images seem to waver between different materials as the streamer onset is brought forth. The differences between uniform and streamer plasma regimes is obvious and the delineation of each arbitrary intensity value works well when comparing similar actuators side by side. Dielectric constant, dielectric thickness, and electrode gap distance were all seen affecting their actuators plasma regime in some way through this method.

CHAPTER V

PARTICLE IMAGE VELOCIMETRY

5.1. Background

The analytical technique commonly referred to as particle image velocimetry (PIV) is the imaging of tracer particles followed by the calculation of their displacements to determine the local fluid velocity [38]. PIV has been seen to provide strong analytical data in the fields of fluid dynamics and essentially any field where flow analysis is deemed useful. Normally, using a high speed and high resolution imaging tool, instantaneous snap shots of a flow may be observed and calculations may be performed. This method of velocity measurement has the pros of non-intrusive seeding, being able to specifically pin point instantaneous points in the flow field, and provides complete control over the observations of specific areas of the flow.

The PIV system normally has two main components: the hardware (or imaging component) and the software (or analysis component). The hardware consists of everything from the seeding particles and light source to the sheet optics and camera. The software consists of the post-processing image analysis that is normally seen in the form of a commercial application or an altered program in a language that can work with image analysis e.g. MATLAB. For PIV

measurements to be accurate, a uniform distribution of seeding at an optimal density along with the correct cross-correlation window shifts are necessary.

5.2. Wall Jet Region

Referred to as a wall jet, the induced flow that a SDBD actuator produces has been researched heavily in the past. A wall jet is simply a flow created when fluid is blown tangentially along a wall. The interesting aspects that surround this phenomenon revolves around the instabilities that are created when a mixing layer is combined with a boundary layer [38]. This yields nonlinearly stable structures for a brief period of time as seen in the example in Figure 28. PIV may be used to observe these structures if the window is zoomed in on areas immediately adjacent to the actuator. If harnessing the power of the actuator's induced flow is the goal, a comprehensive understanding of the mean flow field and structures created by the wall jet is critical.

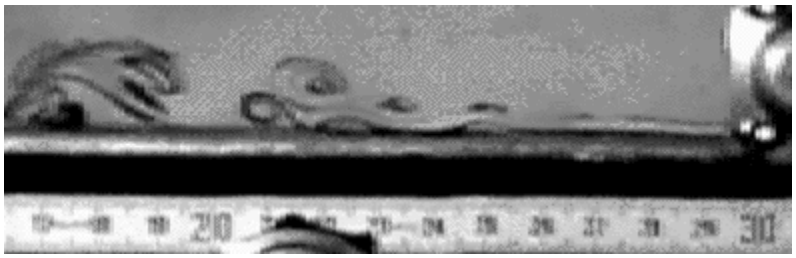

Figure 29. Nonlinearly stable structures formed from a wall jet.

In Figure 29, the area directly above the actuator around the 600 pixel mark on the y-axis is where the wall jet exists. The width of the wall jet extends up to 550-575 pixel marking and extends out for several actuator lengths, slowly decreasing in speed. Complex structures are easily seen in the flow field away from the actuator, but only at a small pulse delay PIV setting does the high speed region become quantifiable. Part of the PIV analysis on the actuators in this experiment will be done focusing on the high speed region.

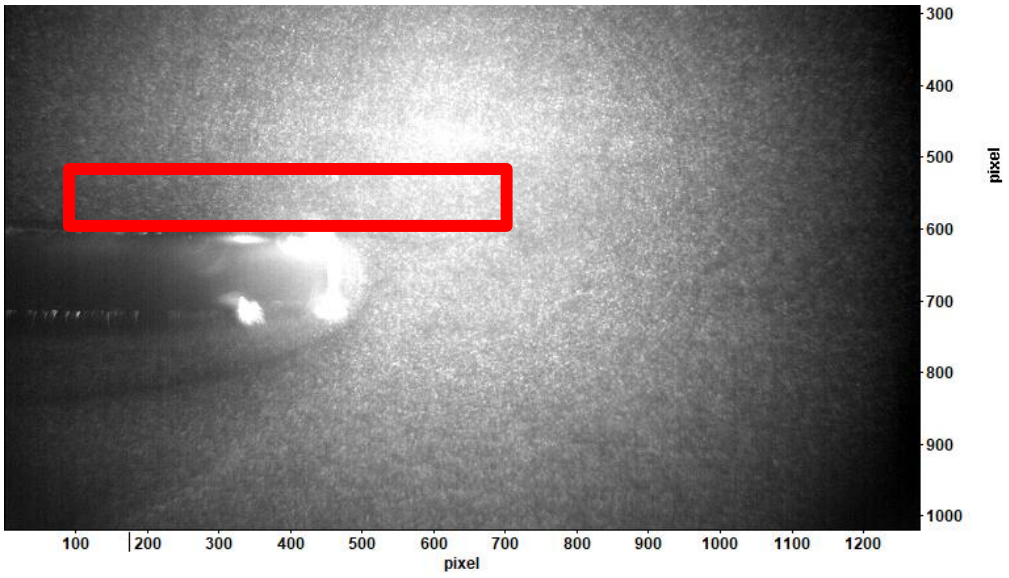

Figure 30. Pre-processed image displaying the location of a wall jet created by the SDBD.

5.3. Experimental Setup

5.3.1. Apparatus Setup and Software Settings

All PIV measurements for this paper was performed using a single setup; the schematics of which are seen in Figure 30. A Taitech DG-100 timing control unit was used to control a Quantum Composers Plus 9518 pulse generator. A Big Sky Laser Ultra Duel Nd:YAG laser was connected to the pulse generator along with a high speed Motion Pro x3 camera. A Tektronix TDS 2014B oscilloscope was connected between the pulse generator and the lasers to monitor their pulse delays. An actuator setup was created consisting of a handmade actuator, a CSI12001X DC regulated power supply, and a custom transformer from Information Unlimited. The power supply runs 1-120 V with an inherent 1 A cap. The transformer is rated for 7 kV and 10 mA. The actuator itself was mounted to an optics bench and covered with a glass aquarium tank. A tube extending from a ChauvetDJ Hurricane 700 fog machine leads into the aquarium to provide the seeding. Two optics lenses were used to focus and spread the laser beam into a laser sheet. A trial and error process was used to determine the laser sheet's minimum thickness with

the laser at approximately 50 cm away from the actuator. The high speed camera was connected directly to a computer that obtains the recording data using a software named MotionStudio and processes the PIV data using a software named DaVis.

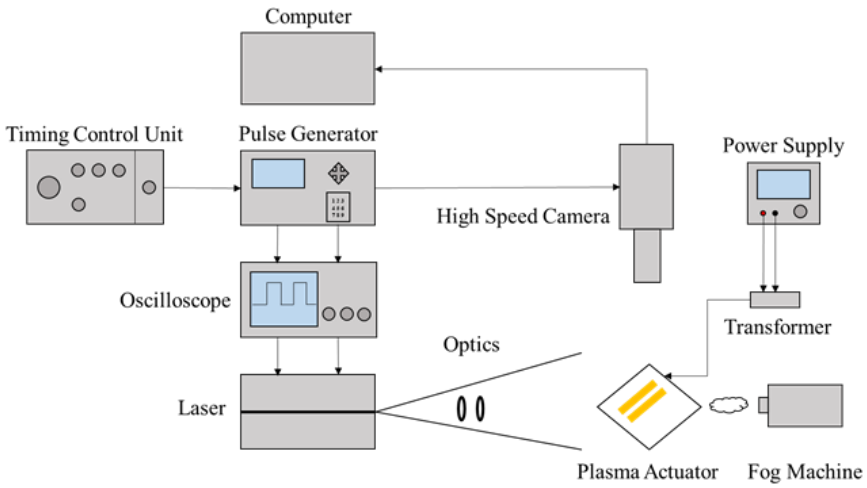

Figure 31. Schematics of PIV setup.

The images are captured with a 250 μs exposure time in double exposure mode at a rate of 250 Hz. The frame sync is set to “external” (the camera) with the sync configuration set to “edge-high” and the trigger configuration set to “rising-edge.” The sharpness has also been increased to 0.1 to aid in distinguishing seeding particles. The camera settings are displayed in the screen captures seen in Figures 31.

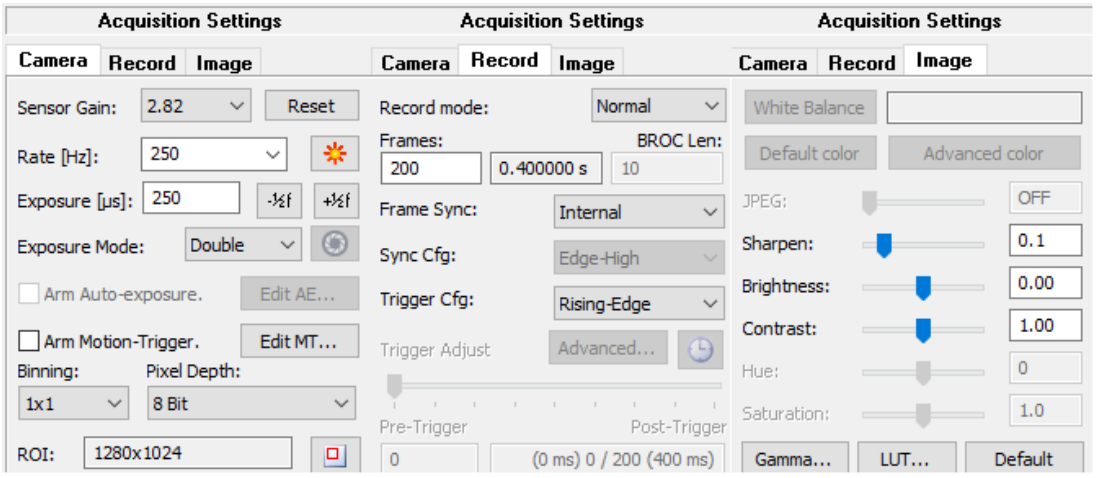

Figure 32. Camera settings as seen in MotionStudio for PIV setup.

In an attempt to meet an accurate PIV scenario, the fog machine was set to pump until the entire aquarium was filled. Then the seeding was allowed to settle until the laser sheet that was centered on the actuator could be clearly seen. To obtain an accurate PIV measurement, pulse delays, or dt, of 500/250/100/50 μs were used in-between camera shots. It was determined that 50 μs was what was necessary to observe an accurate depiction of the high speed region. In Figures 32a-d, the tiny white speck can be seen changing locations between the two raw high speed camera images. This allowed DaVis to accurately calculate the velocity of this area near the actuator. All other dt values resulted in a velocity magnitude at this area of 0. However, to observe a qualitative overall view of the flow, a dt of 500 μs was sufficient as seen in Figure 33.

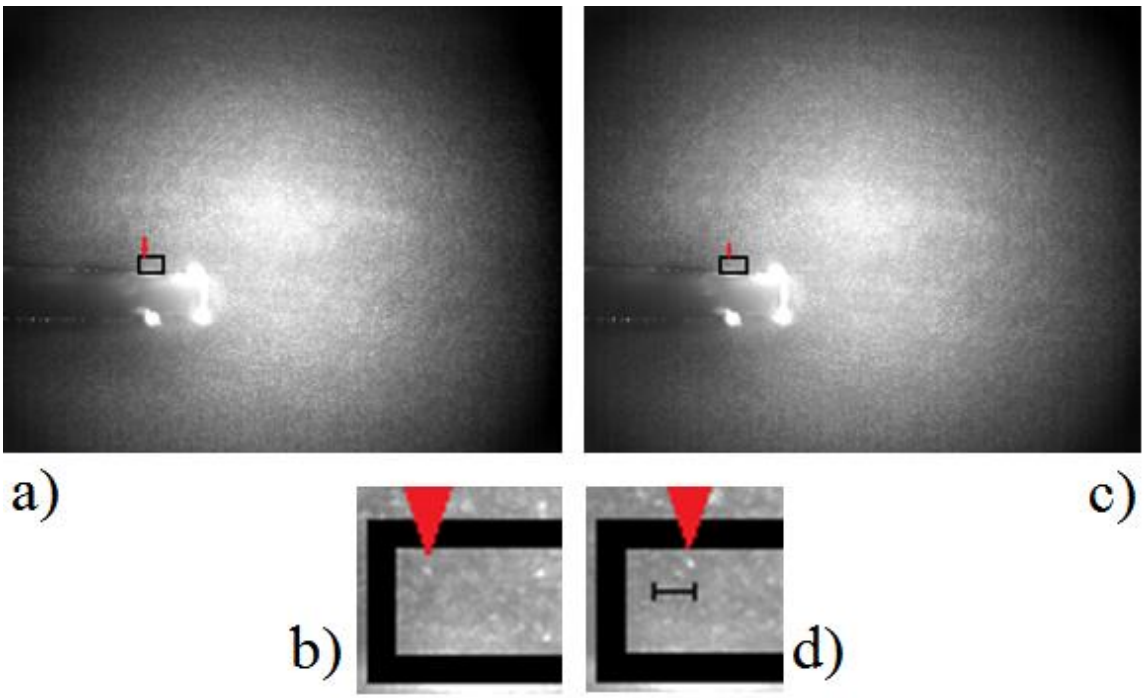

Figure 33. Raw camera images to display particle movement at dt = 50 μs. a) Position 1, b) position 1 zoomed in, c) position 2, d) position 2 zoomed in.

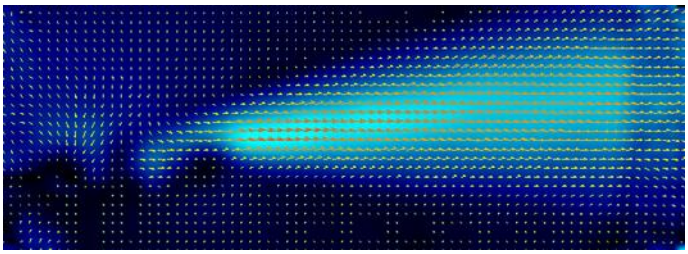

Figure 34. Example PIV image of mean velocity vector field at dt = 500 μs. Colors represents the vector magnitude.

5.3.2. Testing Procedures

The testing procedure started with mounting the designated actuator to the optics bench underneath the glass aquarium. For the PIV measurements, two different procedures were performed. One scenario captured images at dt = 500 μs and enveloped a significantly larger portion of the actuators flow field. The scale is set to 10 pixels. Each actuator was marked with black marker at the point where the laser sheet hits the actuator to reduce the amount of reflection caught by the camera. The main purpose for these tests were to observe the overall flow field and how the changes in parameters affected this field. Seven different actuators were used in this case: acrylic T1G1/T2G1/T3G1/T1G2/T1G3, FR4 T1G1, and alumina T1G1. This was to cycle through the base cases for differences in thicknesses, electrode gap distance, and dielectric materials. Acrylic was the easiest material to work with so it was chosen as the base for both the thickness case and the electrode gap distance case. Each actuator was run at a 0.80 A benchmark for uniformity. The process begins by filling the aquarium with fog and allowing it to settle, actuating the actuator to the correct current, and then capturing 200 images at dt = 500 μs.

In the second scenario, the images were captured at dt = 50 μs dt and at a zoomed in view of the actuator. The scale is approximately 5x the original. The purpose of this procedure was to observe the high speed region, or the wall jet region, of the actuator and potentially calculate velocities coming from the actuator. Only three cases were observed in this wall jet region PIV setup: acrylicT1G1, acrylicT3G3, and FR4T3G3. AcrylicT1G1 was chosen as a base case and

both the acrylicT3G3 and FR4T3G3 were chosen because they were deemed the “best” case (highest theoretical induced flow). The actuators were also run at 0.80 A benchmark for uniformity similar to the previous procedure. This process also begins with filling the aquarium with fog and allowing it to settle, actuating the actuator to the correct current, and hen capturing 200 images but at dt = 50 μs instead.

The PIV post-processing follows a simple flow chart seen in Figure 34. The 200 high speed images are captured with the actuator active. These raw images are imported into DaVis and immediately paired up with its exposure pair, meaning the image count drops to 100 sets. A subtract average time filter is used to remove similar particles in each image. The images are compared to their seven surrounding images. The number of comparative images is arbitrary as tests have shown that in this case five, seven, nine, and comparison between all images given similar results. Upon removing the similar particles, an image similar to Figure 35 remains.

Figure 35. PIV post-processing flow chart.

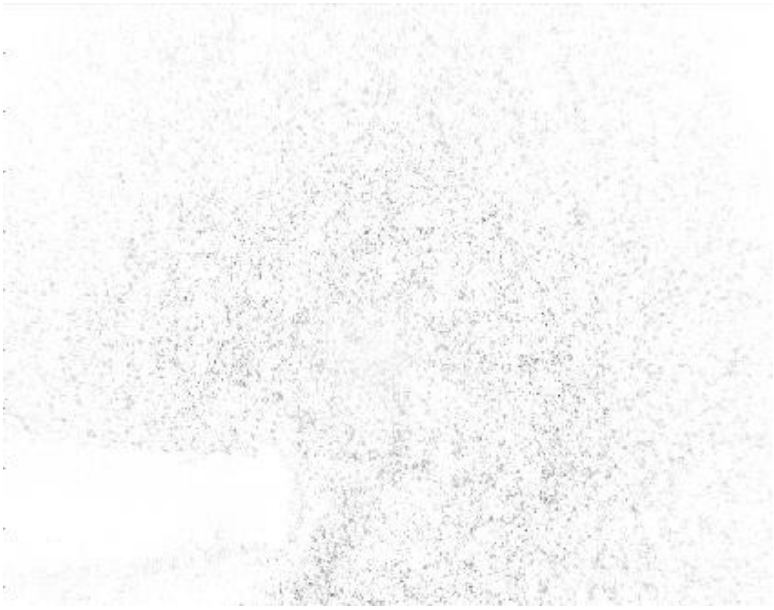

Figure 36. Reverse image of subtract average filtered camera image.

This images are then put through the multi-step PIV processing of DaVis. Firstly, a calibration plate is used to perform image correction on the distortions due to the camera. The calibration plate used is the 058-5 and is seen in Figure 36b. Next, a circular mask is placed around the edges of the images, enabling everything inside and disabling everything outside as seen in Figure 36a. This reduces the amount of noise detected by the program by removing unnecessary darkness due to the camera shutter and plasma actuator before running the PIV process. A multi-pass iteration is done to fine tune the particles over a 256 x 256 50% overlap and a 32 x 32 50% overlap. These window sizes were chosen to meet the situation and accent the particle movements. Processing parameters are displayed in Table 4. Display changes were then used to further accent the change sin velocity between the particles as seen in Figure 37a. Finally, an average and standard deviation calculation was performed on the set of 100 to allow for non-presentational display as well as to give a vague picture of the flow field as seen in Figure 37b. This is useful in seeing how the actuator affects the air around it, but it should be noted that this is not focusing on the high speed jet section immediately next to the actuator.

Table 5. Collection of processing parameters used for the PIV setup in DaVis.

Processing Parameter	Value	Units
CCD pixel dimensions	1280x1024	Pixels
Number of Images	200	Images
Camera delay time (dt)	500/50	μs
Image Exposure Time	250	μs
Capture Rate	250	Hz
Pixel Scale	12	Pixels
Average Subtraction Comparison Set	7	Images
Cross-correlation Window Size level 1	256x256	Pixels
Cross-correlation Window Size level 2	32x32	Pixels

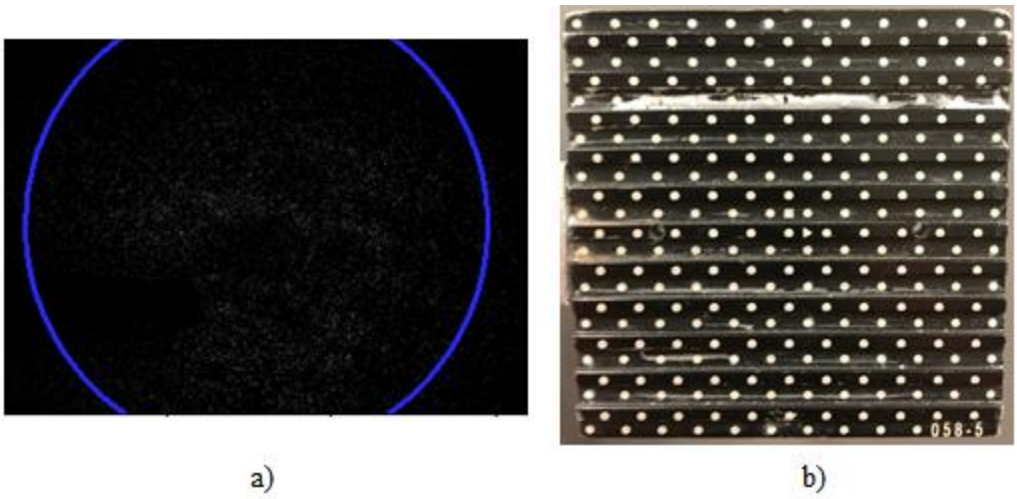

Figure 37. a) Mask defined around the edges of the camera to reduce noise. b) Calibration plate 058-5 used for distortion correction and velocity calculations.

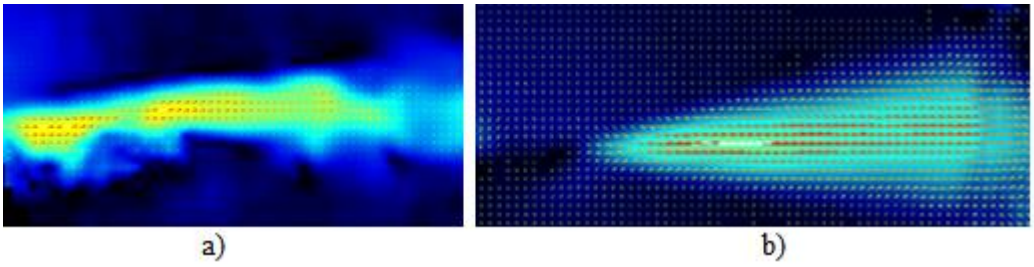

Figure 38. a) Color altered PIV image to accent differences in velocity (AcrylicT1G1). b) Time averaged image of a PIV image set (AcrylicT1G1).

5.4. Analysis of Particle Image Velocimetry

A collection of averaged PIV images is shown. This creates a defect in the images in that in specific window sizes, the complex nonlinear structures in the flow actually cancel out y-velocity components (positive and negative). This leaves a flow that only flows directly away from the actuator. This is not necessarily the case, but it does exhibit where the flow a whole is moving towards.

5.4.1. Qualitative Comparison

(i) Dielectric Type Comparison: There are three main images to observe here: Alumina T1G1, FR4 T1G1, and Acrylic T1G1.

Alumina shows a flatter, tamer, and weaker induced flow hovering around 0.4 m/s. FR4 shows a slightly stronger induced flow that flares out as it extends from the actuator possessing a velocity of around 1.0 m/s. The mean flow fields are displayed in Figure 38.

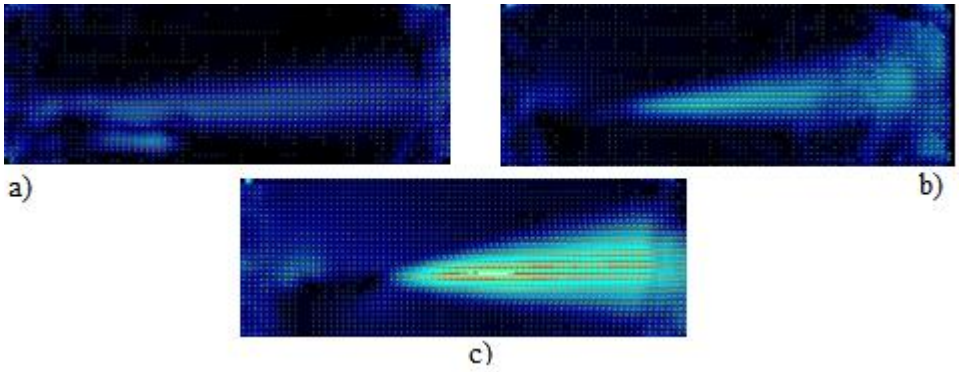

Figure 39. Averaged PIV images. a) AluminaT1G1, b) FR4T1G1, and c) AcrylicT1G1.

(ii) Dielectric Thickness Comparison: The main comparisons here are: Alumina/FR4/Acrylic T1G1, T2G1, and T3G1.

a. Alumina: There were several problems working with alumina. With all the actuators being on the same sheet of alumina back-to-back on the same plane, the flow would be slightly hampered depending on how far back the actuator resides. In addition to this, the thickest sheet was difficult to actuate because the amperage going into it was limited. The sheet itself most likely could have handled a significantly higher voltage but the power supply being used was limiting its potential. The increase in alumina thickness was also quite large, going from 0.63 mm and 1.04 mm to 3.28 mm. This thickness ended up requiring a lot more current to ignite the plasma. This caused the results to be meaningless. With an increase in thickness, there is also an increase in the induced flow strength, but at the cost of requiring more voltage to reach the same current. The induced flow goes from less than 0.4 m/s to 1.0 m/s between the two thicknesses. Figure 39 shows that there is little to no induced flow at all for alumina T3G1 which goes against the previous trend. Simply due

to the incompatibility of the power supply and the thickness of the sheet, any alumina T3 actuator becomes invalid.

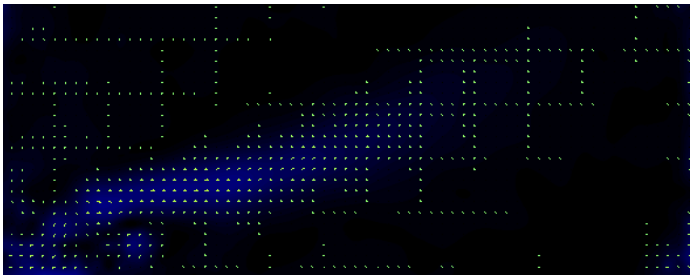

Figure 40. Averaged PIV image of aluminaT3G1 displaying little to no induced flow.

b. FR4: This collection of images is significantly less complex in that the changes are slow and progressive. As the thickness of the FR4 actuators increase from 0.96 mm and 1.58 mm to 3.31 mm, there is a slight but noticeable increase in induced flow strength. The range and spread of the induced flow seems to increase as the thickness increases as well. The velocity vectors go from 0.8m/s up to 1.6 m/s. Circled in red are the points in which the actuator resides. The reflectivity of FR4 was high enough to affect the PIV analysis, meaning the laser physically reflected off of the material and sent a glare into the high speed camera. Sharpie was used to combat this effect, but only reduced the glare marginally. These mean flow field images are presented in Figure 40.

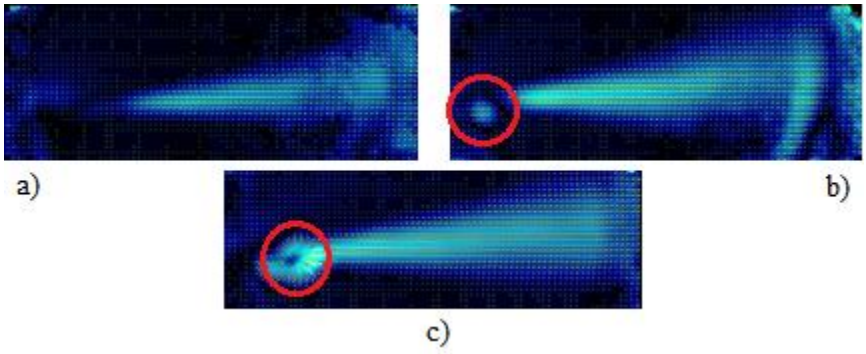

Figure 41. Averaged PIV image comparing thickness differences effect on flow. a) FR4T1G1, b) FR4T2G1, and c) FR4T3G1.

c. Acrylic: As the thickness of acrylic increases, there does not seem to be a discernable pattern. This may be influenced by various things. The thinnest acrylic actuator has a flow field hovering around 1.2 m/s but there are vectors inside the field that spike up to double that velocity. The thickness of the thinnest and second thinnest sheets are relatively close to each other but different, so one would expect similar results. This does indeed happen. The thickest sheet of acrylic with over a 50% increase in thickness yields a very widespread result. The flow velocity itself seems similar to the first two thicknesses but over a wider area.

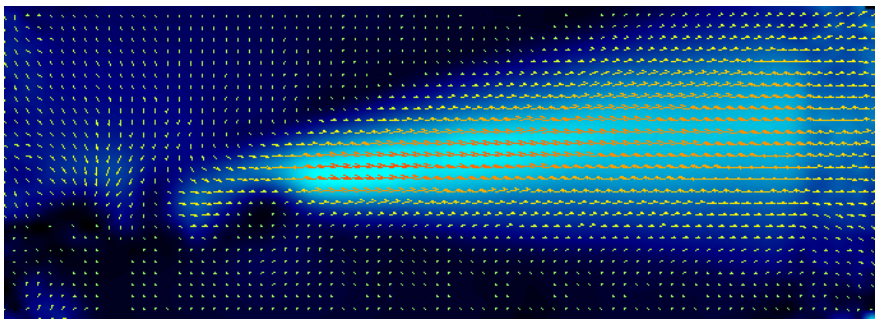

Figure 42. Averaged PIV image of AcrylicT3G1 displaying a widespread flow field.

(iii) Electrode Gap Distance Comparison: The actuators for review are: Acrylic T1G1, T1G2, and T1G3.

a. Acrylic: There is not a huge difference when increasing the gap distance between a 0 mm gap and a 1 mm gap (±0.1). Increasing the gap to 2 mm however creates a completely different flow field. The flow becomes chaotic approximately 75 mm away from the actuator. This value is incidentally the length of the actuators as well. The chaotic flow is seen in Figure 42 and is not only disorganized but has the same vector strength as the previous smooth flow.

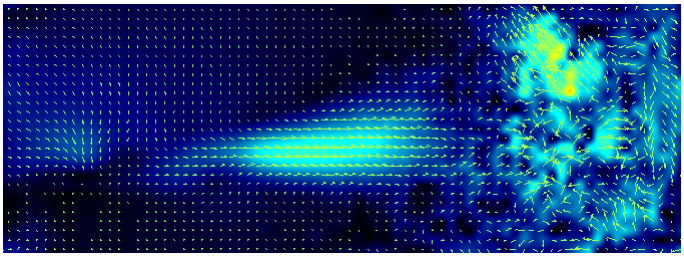

Figure 43. Averaged PIV image of AcrylicT1G3 displaying chaotic flow even after averaging out over several images.

5.4.2. Velocity Growth Analysis

In the second testing scenario described, physical values could be determined from the PIV analysis. In the larger scaled PIV images, the mean flow field was the main result because the resolution was not high enough to determine accurate velocity values from the high speed region. Figure 44 displays one of the jet wall region averaged PIV images. The data used to create this contour plot was extracted and analyzed. Observing that the origin is placed at the back of the exposed electrode, the following plot seen in Figure 45 was created to determine the growth of the induced force. The plot shows velocity profiles cut at intervals 2.5 mm of x moving away from the actuator. Starting on the actuator itself, the flow is not at its strongest, but immediately adjacent to the actuator, the flow hits its highest point as seen from the orange curve for 2.5 mm. Note, this is also the point at which the width of the jet is the thinnest (sharpest). As the profiles move away from the actuator in the +x direction, the profile maximum velocities decrease and expand gradually. When observing Figure 44 from a visual standpoint, the flow field is seen to weaken and expand in the ±y direction which correlates to the plot in Figure 45.

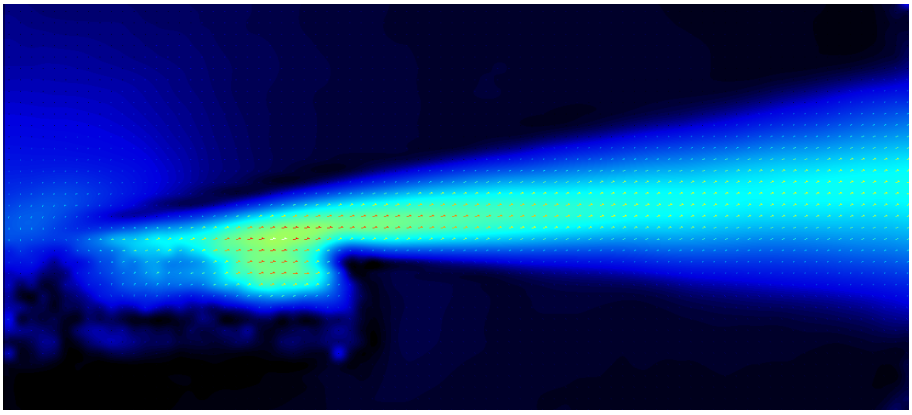

Figure 44. Averaged PIV image of AcrylicT1G1 at 5x zoom of the previous PIV image.

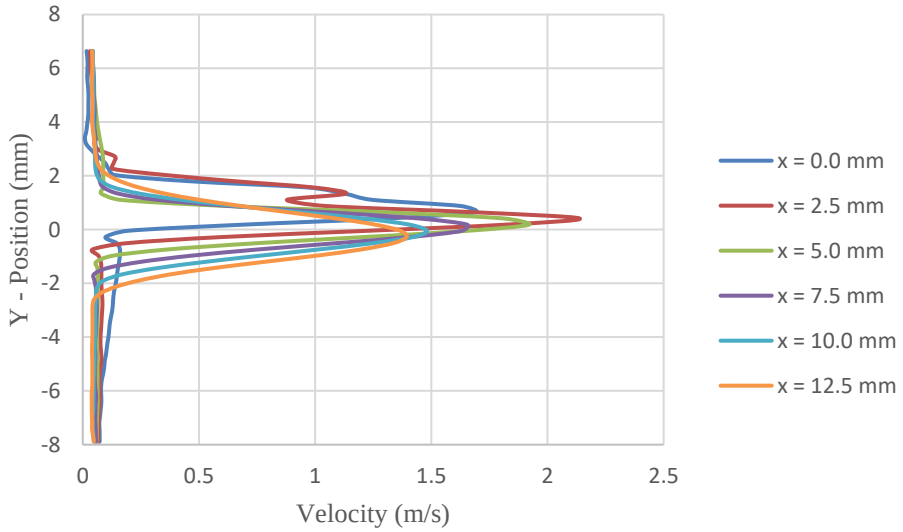

Figure 45. Collection of velocity profiles of AcrylicT1G1 at intervals of 2.5 mm up to 12.5 mm.

When the same process is performed on AcrylicT3G3 (the best acrylic case), a similar trend is seen from the velocity profile. The main difference seems to be a slightly wider expansion of the flow in the ±y direction. The magnitudes of the velocity are similar coming in at 2.0 m/s at maximum. This comparison shows the difference in induced flow strength between no gap distance and a large gap distance along with a relatively significant increase in thickness in acrylic. This data seems to counter previous notions, but at this point amperage, the acrylic base case was reaching its limit (before arcing) while the acrylic best case was still not at its limit.

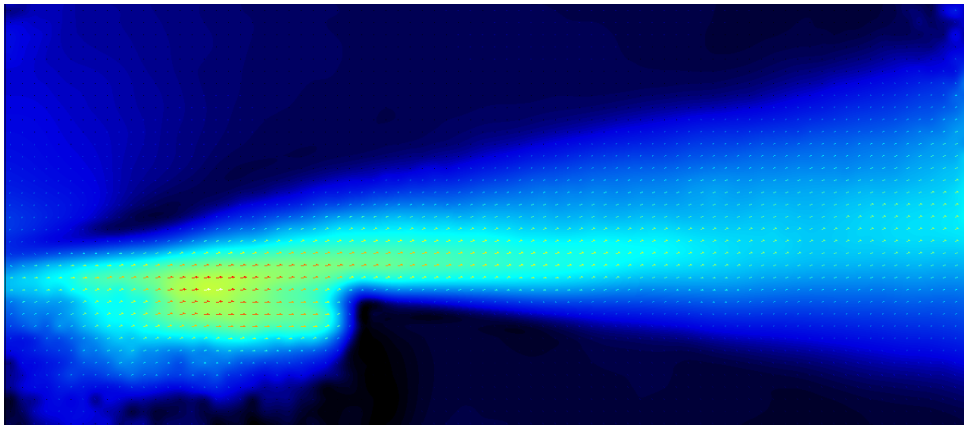

Figure 46. Averaged PIV image of AcrylicT3G3 at 5x zoom of the previous PIV images.

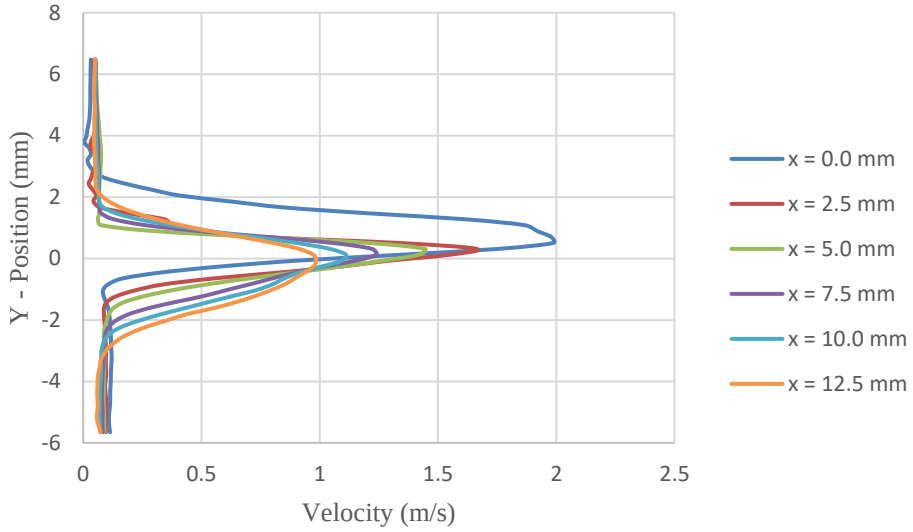

Figure 47. Collection of velocity profiles of AcrylicT3G3 at intervals of 2.5 mm up to 12.5 mm.

Figure 48 and 49 display the same PIV image scaling and velocity profile but for the FR4 best case (FR4T3G3). The most noticeable result of the PIV image is the reflection from the material. This affects the velocity profile as seen by the grey curve at 5.0 mm. By observing the curves not affected by the reflection, the same growth is seen. As the velocity profiles are taken at increasing x positions, the flow is seen to weaken and expand in the ±y direction.

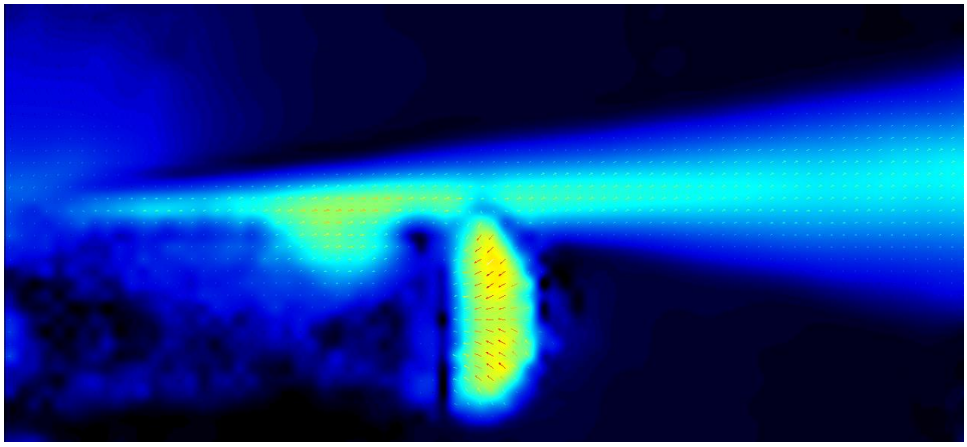

Figure 48. Averaged PIV image of FR4T3G3 at 5x zoom of the previous PIV images.

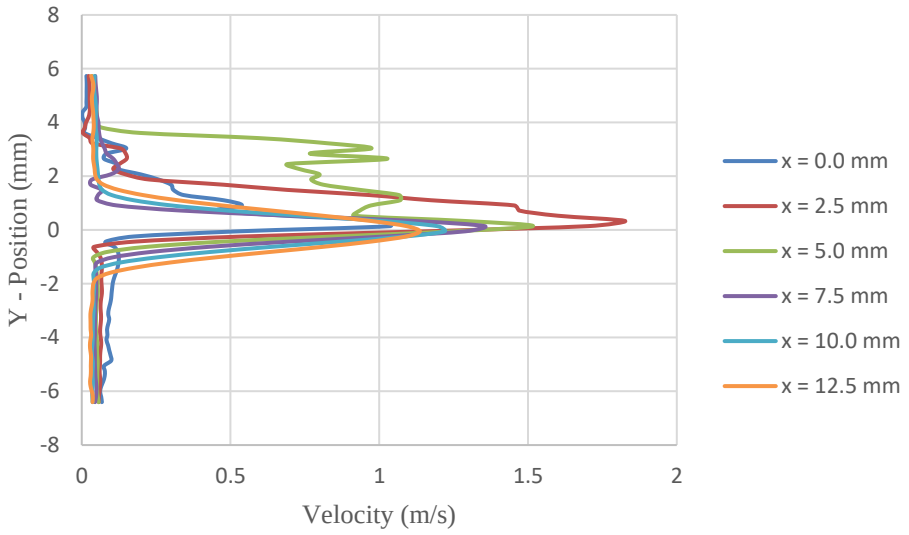

Figure 49. Collection of velocity profiles of FR4T3G3 at intervals of 2.5 mm up to 12.5 mm.

All velocity magnitudes seem to be within a reasonable error margin of each other and even the spread in the y direction is relatively close. This similarity may be caused by the difference in power input into the actuators. These actuators had different power levels input (with the current held the same), but their induced velocities and growths remained the same. This will be taken into consideration when analyzing the effects of dielectric constant, thickness, and electrode gap distance in SDBD actuators.

5.4.3. Induced Flow Mass Analysis

After obtaining velocity values from the wall jet region PIV images, an analysis of the momentum introduced into the flow may be performed. The velocity profile analysis resulted in maximum velocities occurring at approximately 2.5 mm from the actuator origin. By averaging the velocities across the plasma jet, momentum calculations at the point of entrainment may be obtained. Figure 50 clearly shows the sharp increase in velocity due to the entrainment and then the gradual decrease in velocity from the expansion of the flow. The average velocities were calculated starting at the actuator origin and increasing in the +x in intervals of 2.5 mm.

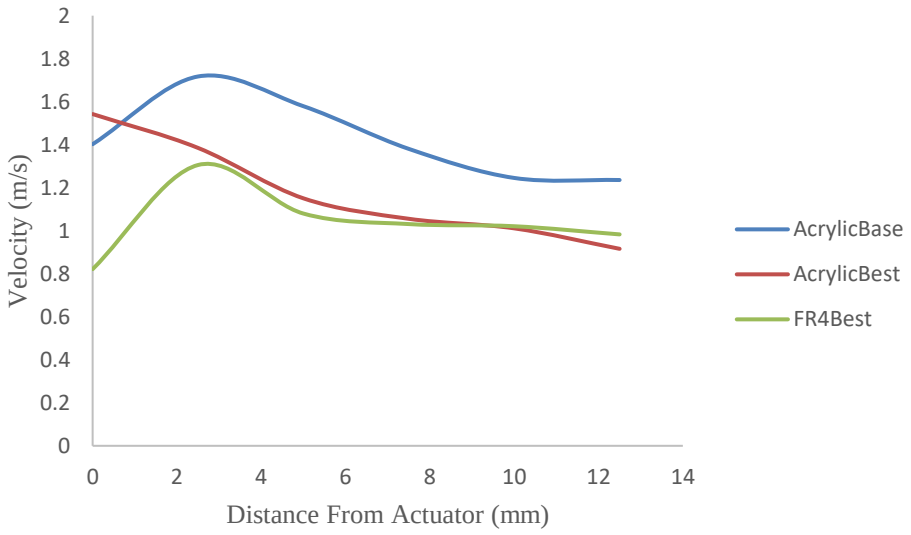

Figure 50. Plot displaying average velocities in respects to their distance from the actuator.

Using the discrete averaged velocity values, the force may be calculated from Equation (8):

$$F = \dot{m}V = \rho A \bar{V}^2 \tag{8}$$

where $\dot{m}$ is the mass flow rate, A is the cross sectional area/surface, and $\bar{V}$ is the average velocity. Figure 51 displays the amount of momentum being introduced into the flow by the plasma actuator along the distance away from the actuator. Note the similarities between Figure 50 and 51. The dependence on the square of velocity intensifies the difference between the actuators.

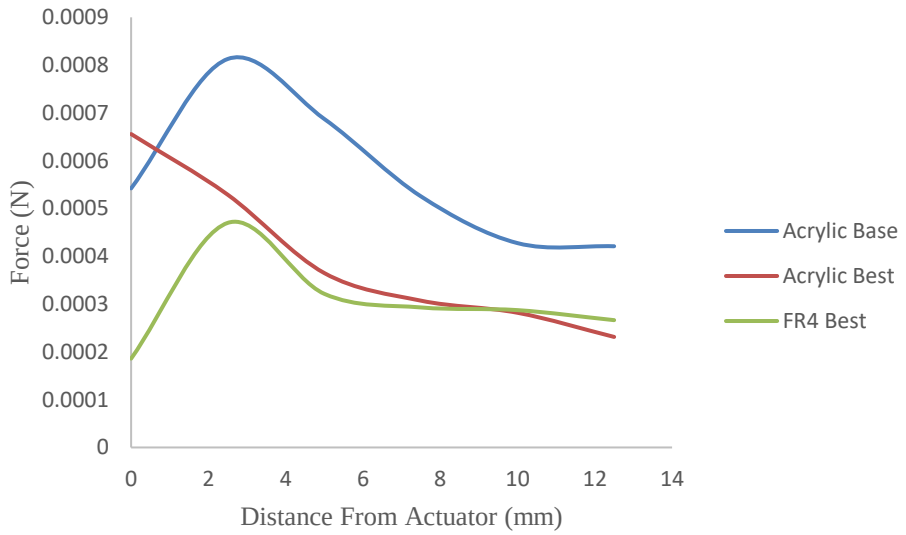

Figure 51. Plot of induced flow strength versus the distance from the actuator.

By specifically observing only x = 2.5 mm (a point immediately adjacent to the actuator), the maximum velocities and thereby the highest force values may be seen in Table 6. From this, a few trends may be discussed. An increase in thickness and gap distance seems to decrease the total amount of momentum being put into the flow. Changing dielectric materials (in this case increasing the dielectric constant) does not seem to have an appreciable effect on the force.

Table 6. List of maximum force values for each actuator case (N).

Actuator Case	Force
AcrylicT1G1	0.0008
AcrylicT3G3	0.0005
FR4T3G3	0.0005

5.5. Uncertainty Sources

Throughout this work several sources of uncertainty were discovered. First, the tool used to measure the electrode gap distances along with the thicknesses for actuators was a Vernier caliper with an uncertainty of ±0.1 mm. The voltage and current indication accuracy values for the DC power supply used is ±1% + 2 digits. Experimental uncertainties came from many places. The fog not being distributed uniformly for PIV measurements cause significant reflections to be seen in certain data sets. Using a larger particle container for testing could aid in having flow that does not affect itself. Although not much, the flow was seen to come out of the actuator, hit the wall of the container, and curve back around eventually. Finding some means of preventing laser reflection from the PIV laser could lead to less noisy results such as non-reflective tape. Different actuators required different camera positioning because of the thickness affecting the place it is held. The wear on actuators created pits and exaggerated already made deformities in the actuators causing unnatural streamers to form. The optics used to focus and spread the PIV laser slowly became burned and clouded which may have altered results. Certain algorithmic uncertainties exist due to using a pre-made trapezoidal integration function on MATLAB and hand calculating velocities from pixel conversion.

5.6. Overall Analysis of Particle Image Velocimetry

Particle image velocimetry was effective at obtaining qualitative and quantitative data. The main issue of this method is performing it with correct conditions. The analysis itself is systematic, but obtaining the pre-processed raw data depends on many variables, for example, the particle dispersion. Having a similar amount of particles consistently was a strong source of error. Outside of this, the analysis provided a lot more physical value to the actuators compared to the OIA. Velocity values for the induced body force was obtained for all the actuators. Many derived quantities could be obtained using only the velocity fields provided by the PIV averaged images.

Additionally, the instantaneous images provided entertaining video footage. Qualitatively, the PIV results could potentially provide footage comparable to Schlieren flow visualization.

CHAPTER VI

CONCLUSIONS

6.1. Conclusions from Analyses

Starting with optical image analysis, trends were observed by altering the dielectric material (the dielectric constant), the dielectric thickness, and the electrode gap distance. The qualitative section of OIA exhibited the SDBD actuators tendencies to change not only their total plasma generated but also the degree of uniformity. When current was held constant, increasing dielectric constant was seen to initiate onset of the uniform plasma regime thus delaying the streamer onset. AcrylicT1G1 was seen as an example where a streamer regime was attained at a current below the maximum benchmark and any additional increase in current would only intensity the streamers. This was not observed from any of the FR4 or alumina cases because their streamer regimes most likely required higher power input than was possible in this test. An increase in thickness was seen to initiate the streamer regime. By increasing the effective distance between the electrodes, the current was forced to take distinct paths causing plasma to form in streamers. This was observed in essentially all scenarios. An increase in electrode gap distance displayed similar results to increasing thickness. The effective distance between the electrodes was increased, thereby causing plasma to form in distinct streamers earlier on in its regime.

A quantitative analysis was performed using the data obtained from the OIA tests. Evaluating the area under the curve created by the plasma intensities yielded results that correlated directly with observations seen in the qualitative analysis. Additionally, total plasma content was calculated using these areas to discover that plasma content was not affected by increasing electrode gap distance, but was inversely affected by increasing dielectric thickness. By holding the current constant, the power fed to each actuator varied causing the thicker dielectric actuators to be starved of enough power to fully actuate. Increasing dielectric constant also had an inversely proportional effect on the total plasma content, seemingly for the same reason as the increasing thickness. Electrode gap distance was theorized to have similar effects as increasing dielectric thickness, bringing up the hypothesis that they might be proportional in the same manner, but the difference in electrode gap distance plasma content was too narrow to view it as much more than error. These results might change in the case of observing more discrete intervals of gap distances. The standard deviation in plasma peaks was calculated to determine uniformity in a quantifiable manner. This analysis resulted in significantly lower standard deviations from FR4 and alumina versus the higher standard deviations from all cases of acrylic. There was a also an increase in standard deviation when observing increased thickness and gap distance, which lines up with streamer onset lowing plasma uniformity.

From the particle image velocimetry study, the first analysis was the qualitative mean flow field analysis. Increasing dielectric constant seemed to have a large inverse effect on the amount of flow created. Being held at the same current, once again, limited the outputs of both FR4 and alumina with the latter being affected more due to its higher dielectric constant. Increasing thickness seemed to produce slightly more induced flow, but still within the realms of uncertainty. Chaotic flow and observed from higher electrode gap distance actuator. From the OIA, it is possible to conclude that increased streamer content could potentially increase flow strength, but at the cost of creating disorderly flow. This lines up with the OIA showing the

streamer formation occurring earlier in the regime due to increased thickness and gap distance. Furthermore, many of the higher thickness and higher gap distance alumina cases were deemed unusable because the power supply could not supply enough power to generate plasma on these actuators.

Additional PIV measurements were performed zoomed in on the actuator in order to obtain more detailed velocity values. The actuators chosen were based off the previous data and which examples displayed the best induced flows i.e. higher thickness and gap distance. This velocity was used to create velocity profiles that displayed changes in the flow as it moves away from the actuator. In all cases, the flow starts at the maximum recorded velocity immediately adjacent to the actuator. As the flow extends away from the actuator, the velocity decreases through expansion. The flow growth analysis in this work showed minimal difference between increases in dielectric constant, thickness, and gap distance, but this is attributed to holding current constant rather than total input power.

Continuing with the observations from these more detailed PIV measurements, the velocity values obtained at x = 2.5 mm (approximate location of highest recorded velocities) were used to estimate maximum momentum transfer. From the three actuator cases chosen for the higher resolution PIV measurements, the base case had the strongest induced body force at 0.8 mN. Increasing thickness and gap distance seems to lower the force which correlates with the previous theory that by holding current constant, the total power given is not enough to satisfy the higher thickness and larger gap distance actuators. These actuators are essentially not performing at their optimal conditions and are being compared to an actuator that is operating closer to its optimal condition (in this case, the acrylic base). The plots created show the sharp rise in velocity in the region immediately adjacent to the actuator. This was followed by a steady decrease in velocity magnitude which coincides with the previous PIV result analysis.

Overall, while not many tangible effects have been discovered to dramatically increase the efficiency of SDBD actuators, several interesting phenomenon have been either observed or gaps have been filled. The main problems seemed to stem from using a power supply that did not meet the demands of the actuators and not having the correct thicknesses/materials to cover a wider spectrum of data points. Additionally, having spare actuators could also aid in solidifying results because the actuators started becoming worn out due to extended usage. As ambiguous as many of the results are, the potential for SDBD actuators should be apparent with the plethora of variables that affect its induced flow. By filling in data points, the relationships between these variables and their effects on induced flow efficiency may be clearly defined.

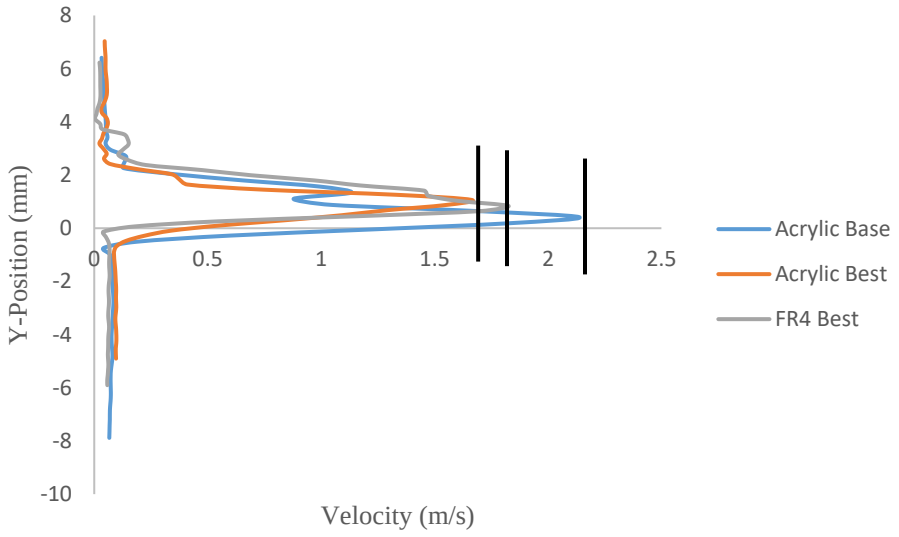

Figure 52. Sample plot displaying velocity profile differences between different actuator cases (x = 2.5 mm).

6.2. Future Works

There are many things that may be done to improve the quality, effectiveness, and scope of the actuators and the experiments used to test the actuators. The most important change is holding input power constant rather than current. This will ensure the comparability between actuator cases. Replacing the power supply to one that can produce higher power but still

maintain the same accuracy would increase the data points for higher dielectric constant and higher thickness materials. Increased data points from a larger variety of dielectric materials (lower dielectric constant like Teflon, a constant between FR4 and alumina like porcelain, and a very large constant) and smaller intervals between dielectric thicknesses/electrode gap distances (between 1.0 mm and 2.0 mm) will significantly lower the amount of ambiguity between the data points present in this work.. Machining actuators rather than hand making them would decrease the variability and inaccuracies in changing electrode gap distance. Having a new actuator for each test case would decrease the chances of pitting and deformities affecting the result. Mounting the high speed camera and actuators in a way so they cannot move could also improve result accuracies.

Additionally, there are many avenues to add onto the three cases discussed in this work. Altering the filament style of the electrodes to increase the total surface area for plasma could potentially have interesting effects such as creating more nonlinear stable structures. A copper ribbon can be used to alter the induced flow and plasma regime. Various interesting geometries can be applied to the actuators to produce additive induced flow. A plethora of geometries can be applied to the addition of multiple actuators to form a thruster system.

Several analysis aspects may be added to improve this work. As stated before, changing the geometric configurations can incorporate thrust vectoring. A capacitive analysis may be performed in an attempt to better understand thickness interactions across dielectric materials. By calculating the capacitance of each actuator, a theoretical analysis may be performed to compare to the actual capacitive effects. A theoretical analysis of efficiency may be performed in the future but it requires measurement of the secondary voltage. In this work, the initial input voltage/current were measured by the power supply but the voltage after the transformer was not. With this information in hand, a comparative analysis of efficiencies between the actuators may be performed.

REFERENCES

[1] Corke, T., et al., *Single Asymmetric Dielectric Barrier Discharge*, Annu. Rev. Fluid Mech. 42:505-29. Web. 27 Oct. 2016.

[2] Pai, K. and J. Jacob, "Asymmetric Surface Dielectric Barrier Discharge as A Novel Method for Biological Decontamination." Ph.D. Dissertation, Mechanical and Aerospace Engineering Dept., Oklahoma State University, Stillwater, OK, 2015.

[3] Pai, K. and J. Jacob, "Evaluation of Dielectric Barrier Discharge Configurations for Biological Decontamination." Master's Thesis, Mechanical and Aerospace Engineering Dept., Oklahoma State University, Stillwater, OK, 2012.

[4] Moreau, E., et al., "Surface Dielectric Barrier Discharge Plasma." ERCOFTAC Bulletin 94.

[5] Fridman, G., et al., "Comparison of direct and indirect effects of non-thermal atmospheric-pressure plasma on bacteria." Plasma Processes and Polymers, 2007, pp. 370-375.

[6] Geuns, R., "The Use of Dielectric Barrier Discharge Plasma Actuators for Low-Speed Flow Control." Master's Thesis, Aerospace Engineering, Delft University of Technology, Delft, Netherlands, 2014.

[7] Lindon, M. and Scime, E., "$C0_2$ dissociation using the Versatile atmospheric dielectric barrier discharge experiment (VADER)." Department of Physics and Astronomy, West Virginia University, Morgantown, WV, 2014.

[8] Mastanaiah, N., “Dielectric Barrier Discharge (DBD) Surface Plasma Sterilization: An In-depth Study of the Factors Contributing to and Enhancing the Sterilization Process.” Ph.D. Dissertation, University of Florida, Gainesville, FL, 2013.

[9] Corke, T., et al., “Order of Magnitude Improvement of SDBD Actuator Effect.” PowerPoint Presentation. 2006.

[10] Orlov, D., “Modelling and Simulation of Single Dielectric Barrier Discharge Plasma Actuators.” Ph.D. Dissertation, Aerospace and Mechanical Engineering, Notre Dame, IN, 2006.

[11] Orlov, D., et al., “Modeling and Experiment of Leading Edge Separation Control Using SDBD Plasma Actuators.” AIAA Paper 2007-0811, 2007.

[12] Orlov, D., Corke, T., and Patel, M., “Electric Circuit Model for Aerodynamic Plasma Actuator.” AIAA Paper 2006-1206, 2006.

[13] Kriegseis, J., et al., “Capacitance and power consumption quantification of dielectric barrier discharge (DBD) plasma actuators.” Journal of Electrostatics, Vol. 69, 2011, pp. 302-312.

[14] Rojas, H. and Jacob, J., “Optical Measurements of Plasma Actuators.” PowerPoint Presentation. 2006.

[15] Little, J., “High-Lift Airfoil Separation Control with Dielectric Barrier Discharge Plasma Actuators.” Ph.D. Dissertation, Mechanical Engineering, Ohio State University, Columbus, OH, 2010.

[16] Berendt, A., et al., "PIV measurements of the flow around airfoil models equipped with the plasma actuator." 16th International Symposium on Applications of Laser Techniques to Fluid Mechanics, Lisbon, Portugal, 2012.

[17] Stix, T. H., "The Theory of Plasma Waves." Literary Licensing, 2012.

[18] Patel, M.P., Ng, T.T., Vasudevan, S., Corke, T.C., Post, M.L., McLaughlin, T.E., and Suchomel, C.F., "Scaling Effects of an Aerodynamic Plasma Actuator," Journal of Aircraft, Vol. 45, No. 1, 2008, pp. 223-236.

[19] Porter, C.O., Baughn, J.W., McLaughlin, T.E., Enloe, C.L., and Font, G.I., "Plasma Actuator Force Measurements," AIAA Journal, Vol. 45, No. 7, 2007, pp. 1562-1570.

[20] Thomas, F.O., Kozlov, A., and Corke, T.C., "Plasma Actuators for Cylinder Flow Control and Noise Reduction," AIAA Journal, Vol. 46, No. 8, 2008, pp. 1921-1931.

[21] Roupassov, D.V., Nikipelov, A.A., Nudnova, M.M., and Starikovskii, A.Y, "Flow Separation Control by Plasma Actuator with Nanosecond Pulsed-Periodic Discharge," AIAA Journal, Vol. 47, No. 1, 2009, pp. 168-185.

[22] Shang, J.S., Kimmel, R.L., Menart, J., and Surzhikov, S.T., "Hypersonic Flow Control Using Surface Plasma Actuator," Journal of Propulsion and Power, Vol. 24, No. 5, 2008, pp. 923-934.

[23] Kasagi, N., Suzuki, Y., & Fukagata, K., "Microelectromechanical systems-based feedback control of turbulence for skin friction reduction," Annual review of fluid mechanics, Vol. 41, 2009, pp. 231-251.

[24] Pinier, J.T., Ausseur, J.M., Glauser, M.N., and Higuchi, H., "Proportional closed-loop feedback control of flow separation," AIAA journal, Vol. 45, 2007, pp. 181-190.

[25] Duchmann, A., Simon, B., Tropea, C., and Grundmann, S., “Dielectric Barrier Discharge Plasma Actuators for In-Flight Transition Delay,” AIAA Journal, Vol. 52, No. 2, 2014, pp. 358-367.

[26] Cliff, J., “The northern US might see a rare aurora borealis,” YouTube, https://www.aol.com/article/2016/04/30/the-northern-us-might-see-a-rare-aurora-borealis/21368259/, April 30th 2016.

[27] nepsleggr1, “Super-Hot Plasma ‘Rain’ Falls On Sun In Amazing Video,” YouTube, February 21st 2013

[28] AdtechEurope, “Plasma Touches Skin – Atmospheric Plasma Touch,” YouTube, 2010.

[29] Advanced Plasma Solutions, “Floating Electrode – Plasma Discharges,” July 19, 2017.

[30] Bittencourt, J.A., “Fundamentals of Plasma Physics,” Springer Science+Business Media LLC, 2004.

[31] Ouellette, J., “Chilling Out with Cold Plasmas,” Scientific American, December 16th 2012.

[32] Santhanakrishnan, A. and Jacob, J.D., “Flow control with plasma synthetic jet actuators,” Journal of Physics D: Applied Physics, October 3rd 2006.

[33] Weiss, R., “Need for Speed,” AIAA Aviation Forum, Keynote Speech, June 6th 2017.

[34] Enloe et al., “Mechanisms and Responses of a Single Dielectric Barrier Plasma Actuator: Plasma Morphology,” AIAA Journal, Vol. 31, No. 3, March 2004.

[35] Balanis, C.A, “Advanced Engineering Electromagnetics,” John Wiley & Sons, 2012.

[36] Dai, X. and Roth, J.R., "Induced flow direction of a single ehd plasma actuator using the one atmosphere uniform glow discharge plasma," IEEE Conference, June 4th 2006.

[37] Rossi, L.F., "Vortex Computations of Wall Jet Flows," Forum on Vortex Methods for Engineering Applications, Albuquerque NM, Sandia National Laboratories, December 22nd 1994.

[38] Kiger, K., "Introduction of Particle Image Velocimetry," University of Maryland, Burgers Program for Fluid Dynamics, College Park, Maryland, May 24th.

APPENDIX

MATLAB Intensity Program:

```
[FileName,PathName] = uigetfile({'*.jpg';'*.JPG';'*.jpeg';'*.JPEG'},'Select any JPEG image');
y=fullfile(PathName,FileName);
a=imread(y,'jpg');
figure(1)
image(a)
b=(double(a(:,:,1))+double(a(:,:,2))+double(a(:,:,3)))/3;
figure(2)
colormap(gray)
imagesc(b)
[x,y] = size(b);
Values = zeros(x,y);
Result = zeros(1,y);
for i = 1:y
   sum = 0;
   for j = 1:x
      sum = sum + b(j,i);
   end
   Result(1,i) = sum/x;
end
figure(4)
plot(Result,'b')
axis([0 4000 0 16]);
xlabel('Pixel Column')
ylabel('Average Intensity')
```

VITA

Alvin Dinh Ngo

Candidate for the Degree of

Master of Science

Thesis: INVESTIGATION OF SCALING EFFECTS DUE TO VARYING DIELECTRIC MATERIALS IN ASYMMETRIC SURFACE DIELECTRIC BARRIER DISCHARGE ACTUATORS

Major Field: Mechanical and Aerospace Engineering

Biographical:

Education:

Completed the requirements for the Master of Science in Mechanical and Aerospace Engineering at Oklahoma State University, Stillwater, Oklahoma in July, 2017.

Completed the requirements for the Bachelor of Science in Aerospace Engineering at University of Oklahoma, Norman, Oklahoma in May, 2015.

Experience:

Research Assistant at University of Oklahoma, Norman, Oklahoma

Research Assistant at Oklahoma State University, Stillwater, Oklahoma

Professional Memberships:

AIAA